Journal of Geophysical Research: Oceans

RESEARCH ARTICLE
10.1029/2017JC013173

Zonally Elongated Transient Flows: Phenomenology and Sensitivity Analysis

M. V. Rudko[1,2,3], I. V. Kamenkovich[1], M. Iskadarani[1], and A. J. Mariano[1]

[1]Department of Ocean Sciences, RSMAS/University of Miami, Miami, FL, USA, [2]Now at Cooperative Institute for Marine and Atmospheric Studies, University of Miami, Miami, FL, USA, [3]Now at Atlantic Oceanographic and Meteorological Laboratory, National Oceanic and Atmospheric Administration, Miami, FL, USA

Key Points:
- Anisotropy of mesoscale variability
- The impact of environmental parameters on oceanic anisotropy

Correspondence to:
M. V. Rudko,
mrudko@miami.edu

Citation:
Rudko, M. V., Kamenkovich, I. V., Iskadarani, M., & Mariano, A. J. (2018). Zonally elongated transient flows: Phenomenology and sensitivity analysis. *Journal of Geophysical Research: Oceans*, *123*, 3982–4002. https://doi.org/10.1029/2017JC013173

Received 7 JUN 2017
Accepted 24 APR 2018
Accepted article online 26 APR 2018
Published online 8 JUN 2018
Corrected 28 SEP 2018

This article was corrected on 28 SEP 2018. See the end of the full text for details. All corrections have been made to the online version.

Abstract This study explores the phenomenology of zonally elongated transients (ZELTs) in the ocean and the sensitivity of their properties to changes in several environmental factors. ZELTs explain a major part of anisotropy in mesoscale turbulent flow. Calculations are performed in a two-layer, quasi-geostrophic model. Empirical Orthogonal Functions (EOF) decomposition allows for the separation of ZELTs from the background turbulent flow as several leading EOF modes. The leading Extended EOF reveals that ZELTs propagate westward at the speed of $\sim$1 cm s^{-1}. The decrease in the planetary vorticity gradient and increase in the bottom drag coefficient each leads to flattening of the variance spectrum, isotropization of the leading EOF, and fast decay of the autocorrelation function of its corresponding Principal Component.

1. Introduction

Satellite observations and numerical model simulations reveal a series of zonally elongated transient flow patterns populating every basin of the World Ocean (Maximenko et al., 2005). We refer to these flow structures as zonally elongated transients or ZELTs (Kamenkovich et al., 2015). Anisotropic and nonuniform distribution of Eulerian (Huang et al., 2007; Scott et al., 2008; Stewart et al., 2015) and Lagrangian (Kamenkovich et al., 2015; Laurindo et al., 2017; Rypina et al., 2012) statistics further suggests that ZELTs exhibit a significant spatial variability over different parts of the World Ocean. The present article focuses on two aspects of ZELTs: first, their proper identification and separation from the background flow, and second, their sensitivity to and dependence on environmental parameters.

Multiple, predominantly zonal oceanic flows are detected in time-mean sea surface height (Maximenko et al., 2008) and Argo data (Van Sebille et al., 2011). These flow structures are claimed to be the counterparts of stationary jets observed in the atmospheres of giant planets (Galperin et al., 2004; Williams, 1975). However, most of the kinetic energy at the mesoscale in the ocean is contained in the time-evolving flow anomalies (Zang & Wunsch, 2001). Averaged over 18–200 weeks, these flow anomalies reveal the presence of low-frequency zonally elongated flow patterns (Maximenko et al., 2005). On the other hand, even randomly distributed westward propagating vortices can appear as zonally elongated flow patterns in time-averaged fields (Schlax & Chelton, 2008). Although Buckingham and Cornillon (2013) and Chen et al. (2016) argue that randomly distributed propagating eddies cannot explain the entire signal associated with anisotropic flow patterns, the time-averaging does not seem to be a reliable tool for identifying ZELTs.

Zonally elongated flow structures can also be isolated from the background flow by applying spatial Fourier filtering (Kamenkovich et al., 2015; Maximenko et al., 2008). However, the spatial Fourier spectrum of oceanic turbulence is broadband (McWilliams, 2008); the lack of scale separation between different flow components renders the Fourier filtering inefficient in that there is no clear choice for the cut-off wave number. To this end, the problem of efficient ZELTs extraction becomes equivocal: both time-averaging and spatial Fourier filtering can produce spurious flow patterns. A double-spectral approach seems to be an appealing remedy to this problem (Ivanov & Collins, 2009). The approach consists of dividing a data set into several frequency bands by means of wavelet transform to apply spatial Fourier decomposition within each of the bands. Ivanov et al. (2012) find that zonally elongated flow patterns have a dominant period greater than 2.5 years. While such an approach certainly helps to identify the time scale, as mentioned above, spatial Fourier decomposition precludes unambiguous detection of a particular flow pattern.

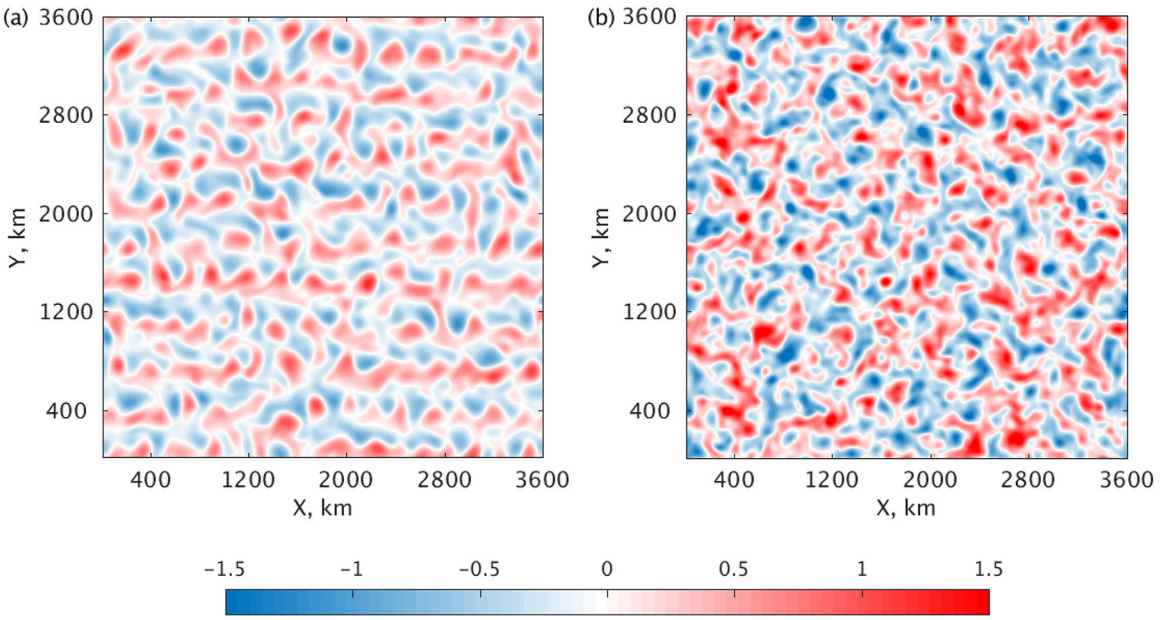

Figure 1. Upper-layer snapshots of the velocity stream function $\times 10^4$ of simulated (a) anisotropic and (b) isotropic turbulent flows.

Many environmental parameters can influence the variability of oceanic turbulence and its associated anisotropy, including Earth's rotation, stratification, and dissipative processes. Simulations of geostrophic turbulence suggest that varying bottom friction causes a 10-fold change in the magnitude of the stationary zonal jets; a less pronounced effect is observed due to variations in lateral friction (Berloff et al., 2011). The anisotropy of the time-variable flow associated with ZELTs, on the other hand, can respond differently to variations in friction. The impact of Earth's rotation (β-effect) and stratification on the anisotropy of ocean variability also remains unknown.

We perform simulations in a two-layer quasi-geostrophic model. This model is conceptually simple yet represents the essential dynamics well; furthermore, its computational efficiency allows an efficient exploration of the model's parameter space. A more complex and costly model would be impractical computationally because of the long integration times required for each numerical simulation. The details of the numerical model are provided in section 2. By applying Fourier and EOF decomposition to simulated isotropic and anisotropic turbulent flows, we demonstrate that EOF decomposition is a more appropriate technique to

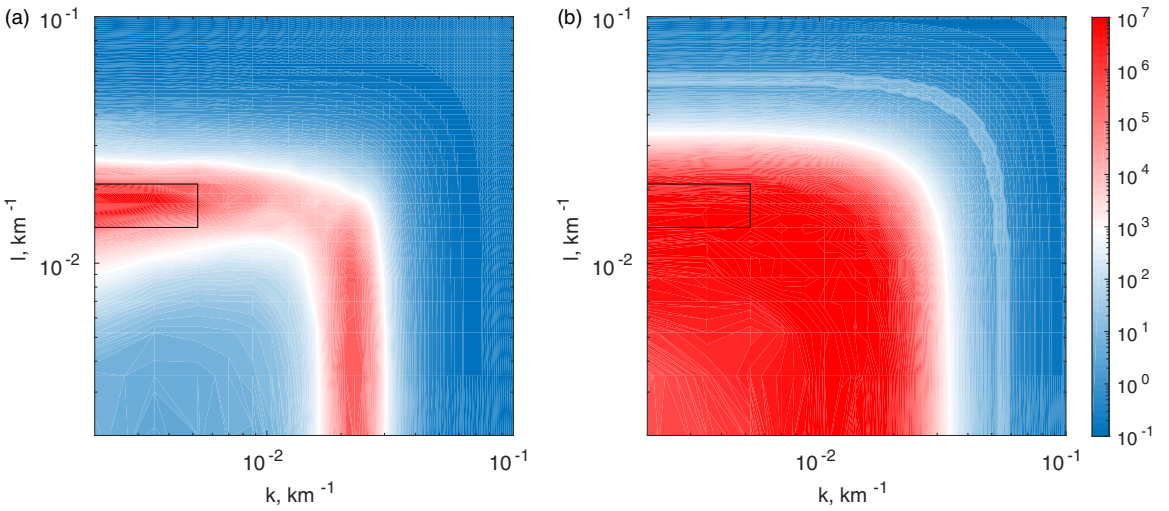

Figure 2. Upper-layer spatial Fourier spectra of the velocity stream function of simulated (a) anisotropic and (b) isotropic turbulent flows. Rectangle denotes the range of wave numbers within which Fourier filter is applied (see the text).

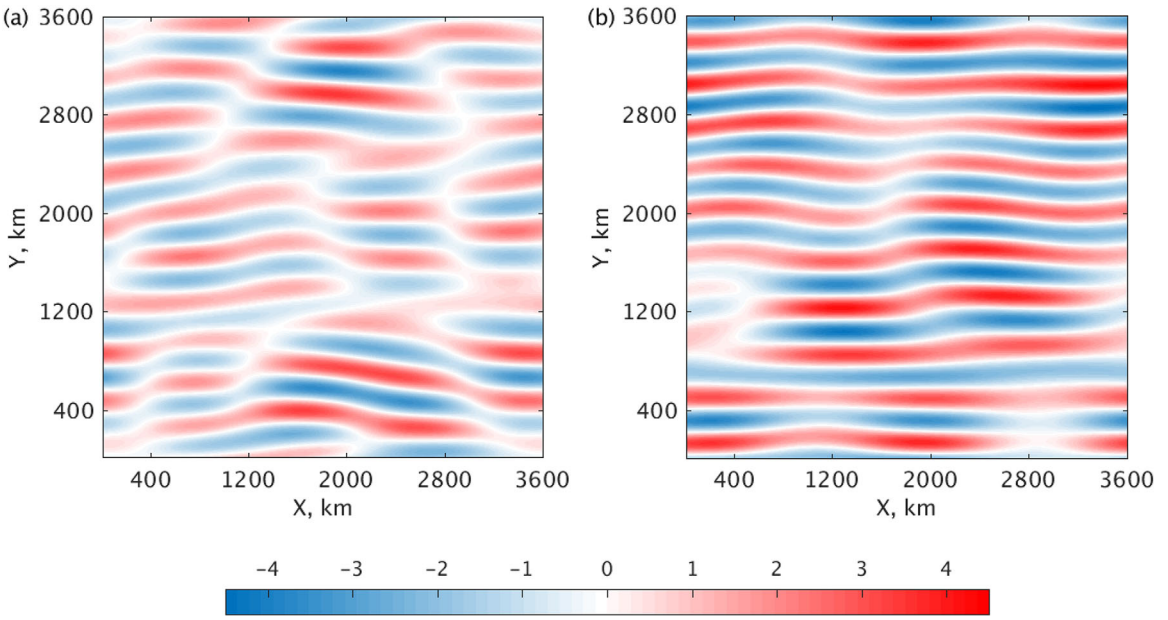

Figure 3. Low-passed Fourier filtered velocity stream function $\times 10^3$ of simulated (a) anisotropic and (b) isotropic turbulent flows.

identify ZELTs. We then quantify the propagation of ZELTs by means of the Extended EOF decomposition. We compare the variance spectrum, the leading EOF and autocorrelation function (ACF) of the corresponding Principal Component (PC) for several values of β and bottom drag coefficient. Finally, we quantify the sensitivity of the anisotropy associated with the leading EOF to simultaneous variations in β and bottom drag coefficient by constructing a response surface in β-bottom drag parameter space.

2. Numerical Model and Experiment Design

The governing equations of the two-layer quasi-geostrophic model are the conservation of potential vorticity in each layer (Pedlosky, 2013) with added forcing and viscous terms:

$$\frac{\partial q_1}{\partial t} + J(\psi_1, q_1) = F + \nu \nabla^4 \psi_1 \tag{1}$$

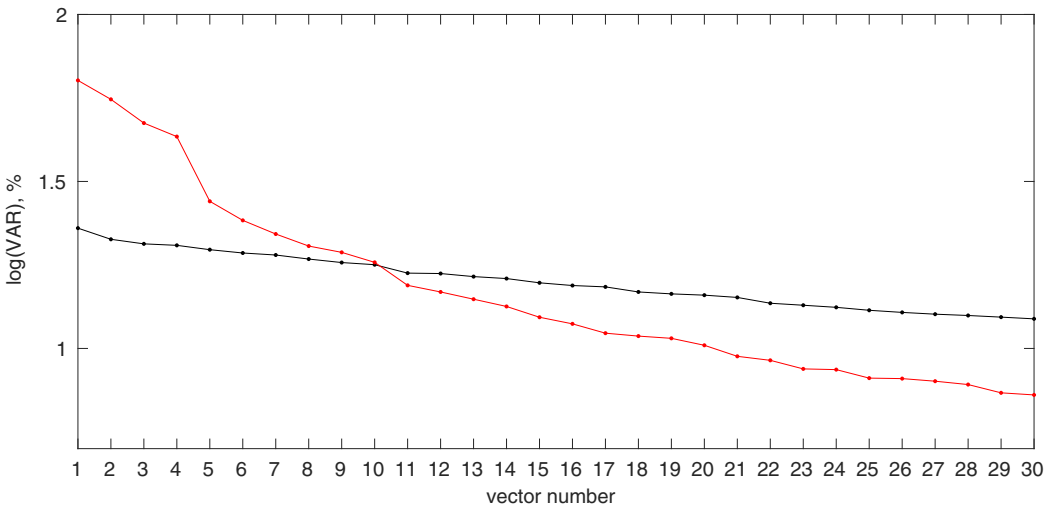

Figure 4. Amount of explained variance by 30 leading EOF modes of simulated anisotropic (red curve) and isotropic (black curve) turbulent flows.

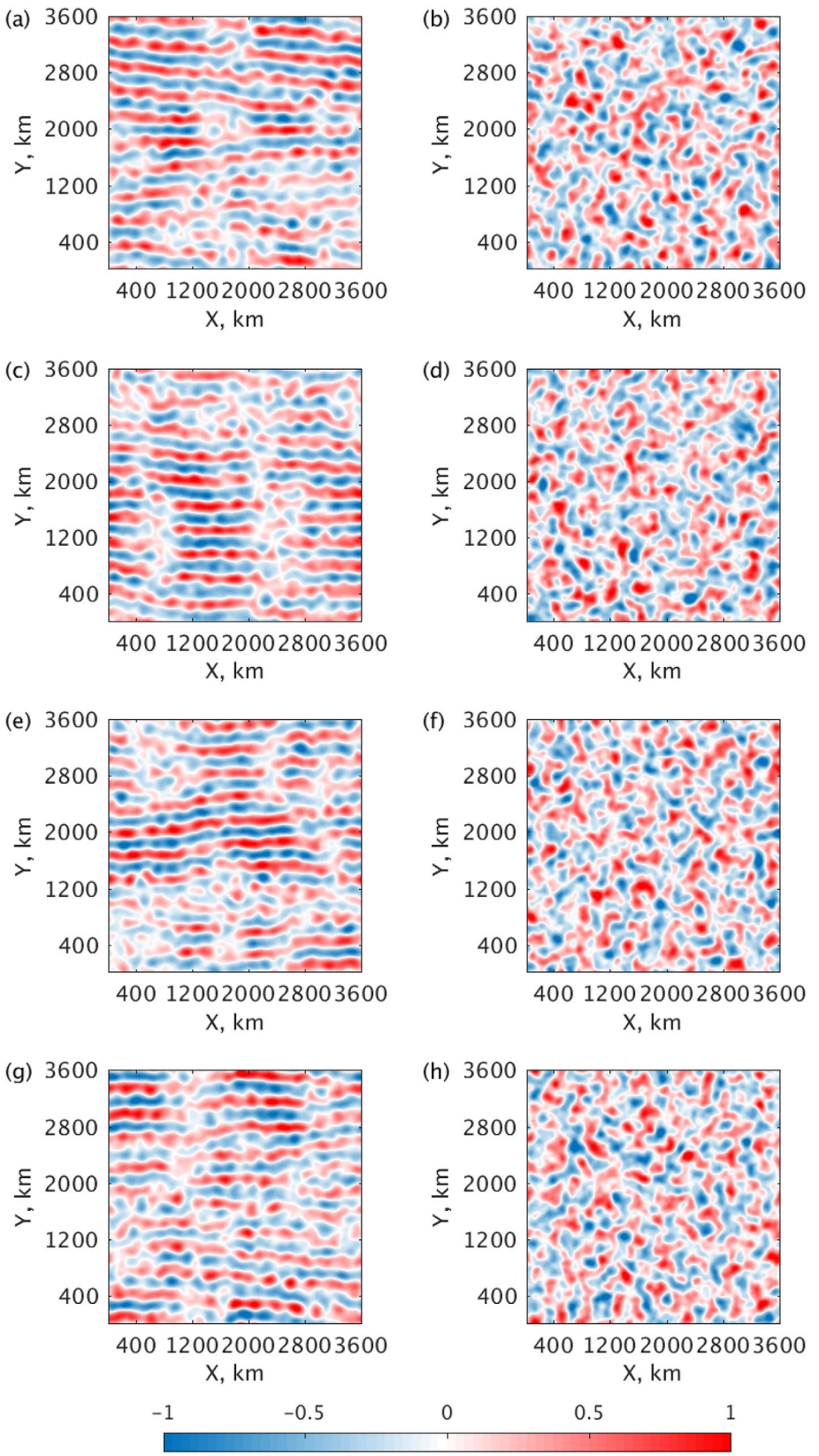

Figure 5. The first four leading EOFs$\times 10^{-3}$. Left column: anisotropic turbulent flow. Right column: isotropic turbulent flow. (a and b) EOF1, (c and d) EOF2, (e and f) EOF3, and (g and h) EOF4.

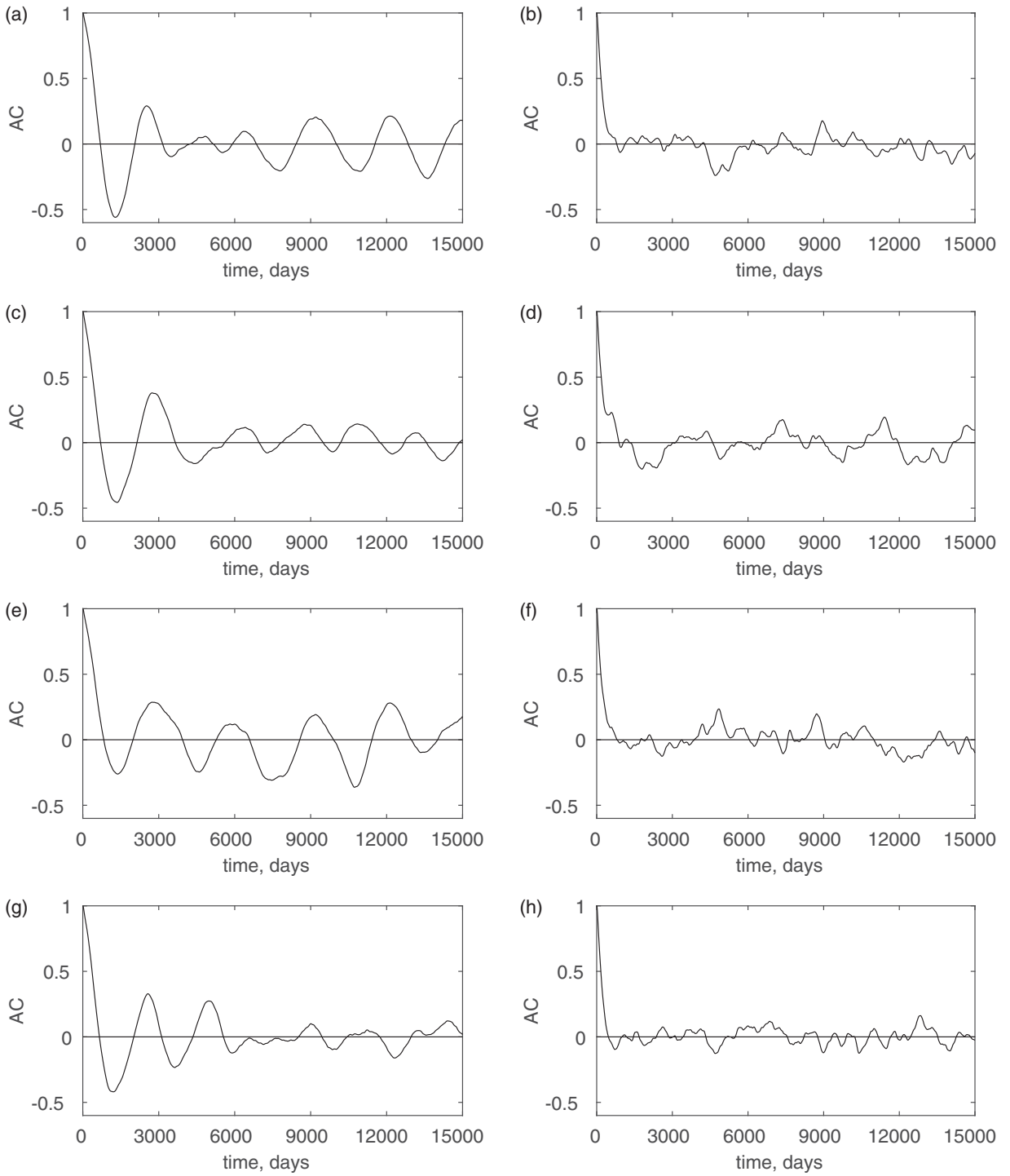

Figure 6. ACF of PCs corresponding to several leading EOF modes. Left column: anisotropic turbulent flow. Right column: isotropic turbulent flow. (a and b) PC1, (c and d) PC2, (e and f) PC3, and (g and h) PC4.

$$\frac{\partial q_2}{\partial t} + J(\psi_2, q_2) = -\gamma \nabla^2 \psi_2 + \nu \nabla^4 \psi_2 \tag{2}$$

Here ψ_n is the stream function in layer n, $n = 1, 2$ (hereafter, indices 1 and 2 refer to the top and bottom layers, respectively), $J(\psi_n, q_n) = \frac{\partial \psi_n}{\partial x}\frac{\partial q_n}{\partial y} - \frac{\partial \psi_n}{\partial y}\frac{\partial q_n}{\partial x}$ is the Jacobian operator, ν is a lateral eddy viscosity, γ is a

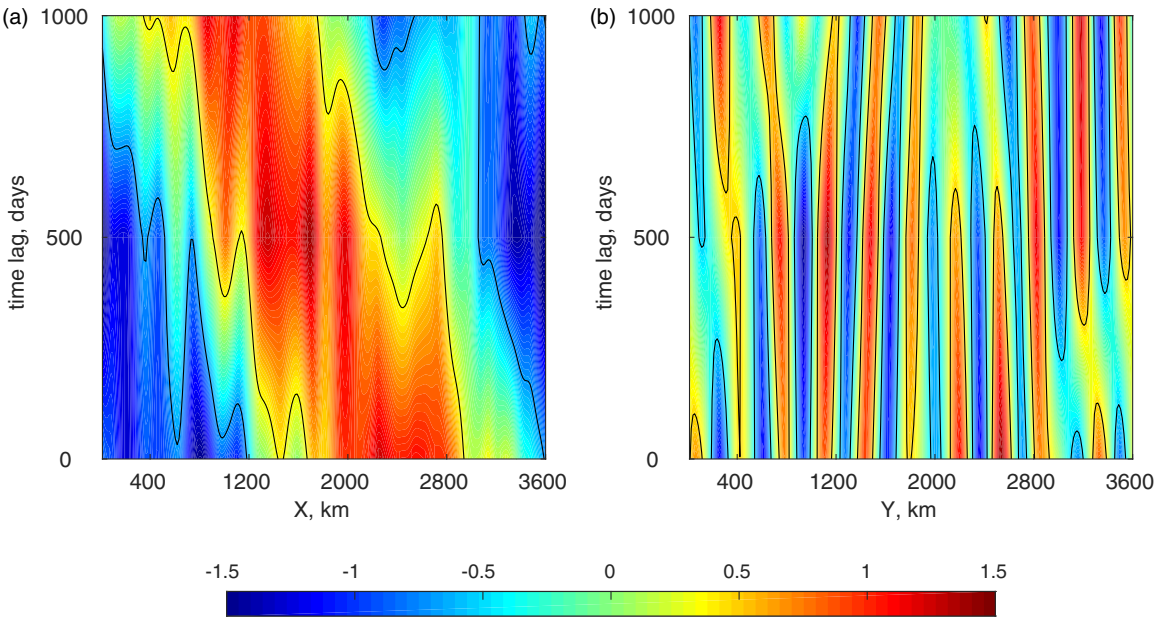

Figure 7. Extended EOF1 $\times 10^{-3}$ along (a) zonal direction and (b) meridional direction as a function of time lag.

bottom drag coefficient, and F is the forcing function. Potential vorticity is related to the stream function in each layer by

$$q_1 = \nabla^2\psi_1 + S_1(\psi_2 - \psi_1) + \beta y$$

$$q_2 = \nabla^2\psi_2 + S_2(\psi_1 - \psi_2) + \beta y$$

where β is the north-south gradient of planetary vorticity, $S_1 = \frac{f_0^2}{H_1 g_1'}$ and $S_2 = \frac{f_0^2}{H_2 g_1'}$ are the stratification parameters, and f_0 is the reference value of the Coriolis parameter.

For anisotropic turbulence simulations, the model was forced by a horizontally homogeneous, baroclinically unstable flow with zonal velocity U in the top layer only (Haidvogel & Held, 1980). In this case, the model can be written as

$$\frac{\partial \xi_1}{\partial t} + J(\psi_1, \xi_1) + (\beta + S_1 U)\frac{\partial \psi_1}{\partial x} = -U\frac{\partial \xi_1}{\partial x} + \nu\nabla^4\psi_1 \quad (3)$$

$$\frac{\partial \xi_2}{\partial t} + J(\psi_2, \xi_2) + (\beta - S_2 U)\frac{\partial \psi_2}{\partial x} = -\gamma\nabla^2\psi_2 + \nu\nabla^4\psi_2 \quad (4)$$

where

$$\xi_1 = \nabla^2\psi_1 - S_1(\psi_1 - \psi_2)$$

Table 1
Values of Different Parameters for 1-D Sensitivity Analysis

(β, m^{-1}s^{-1}; γ, s^{-1})	# of EOF modes with $\alpha \geq 0.6$	$\sqrt{\left(\frac{\mathrm{EOF}_t}{\mathrm{EOF}_c}\right)^2}$	(β, m^{-1}s^{-1}; γ, s^{-1})	# of EOF modes with $\alpha \geq 0.6$	$\sqrt{\left(\frac{\mathrm{EOF}_t}{\mathrm{EOF}_c}\right)^2}$
(2.15; 1)	3	1.01	(1.14; 5)	0	0.47
(2.15; 2)	0	0.82	(1.47; 5)	0	0.43
(2.15; 3)	9	0.58	(1.75; 5)	0	0.40
(2.15; 4)	11	0.49	(1.98; 5)	0	0.39
(2.15; 7)	0	0.37	(2.15; 5)	5	0.38
(2.15; 9)	0	0.34	(2.25; 5)	7	0.37

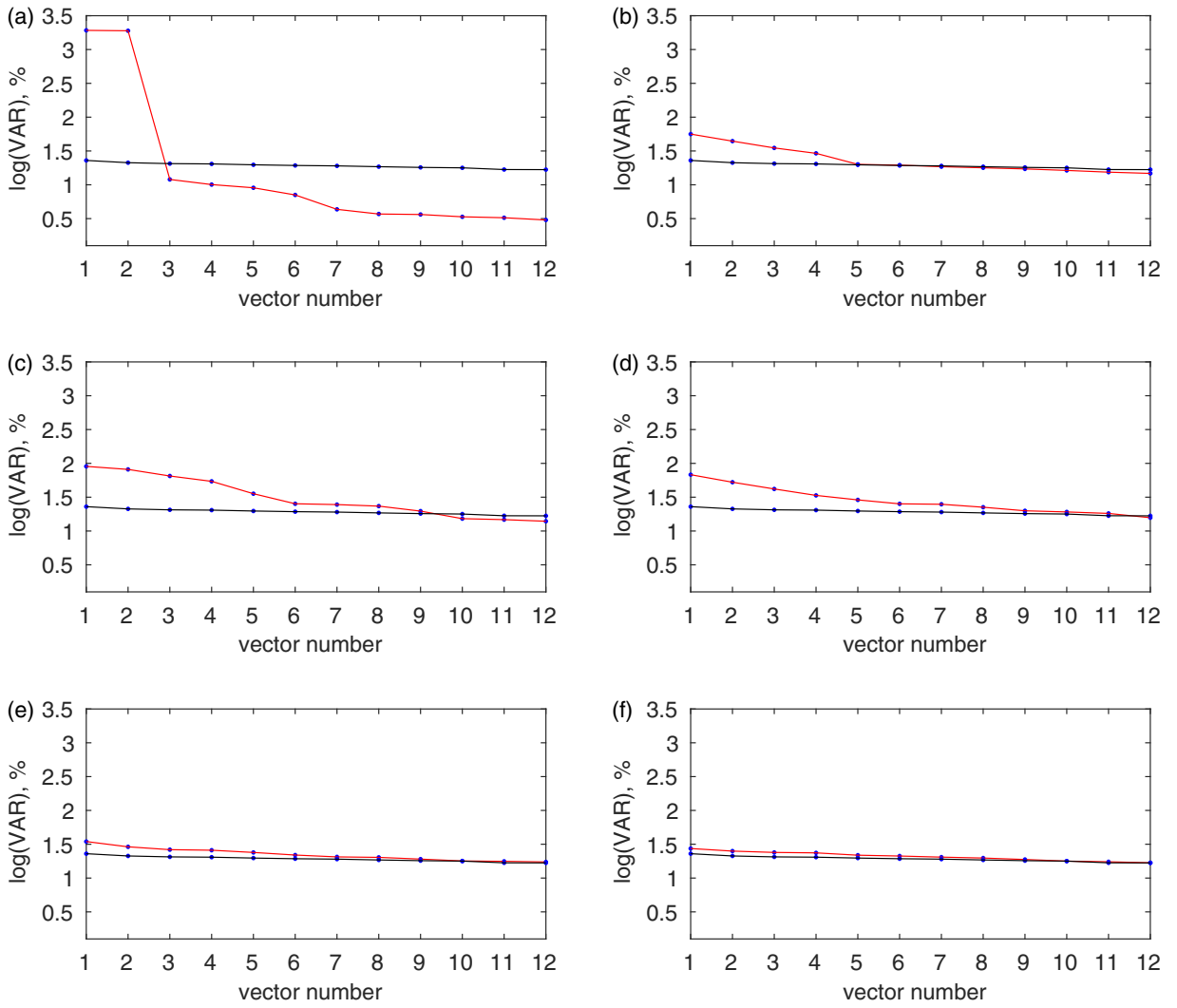

Figure 8. Amount of explained variance by 12 leading EOF modes of simulated anisotropic turbulent flow for $\beta=2.15\times10^{-11}$ m^{-1} s^{-1} (red curves) and (a) $\gamma=1\times10^{-7}$ s^{-1}, (b) $\gamma=2\times10^{-7}$ s^{-1}, (c) $\gamma=3\times10^{-7}$ s^{-1}, (d) $\gamma=4\times10^{-7}$ s^{-1}, (e) $\gamma=7\times10^{-7}$ s^{-1}, and (f) $\gamma=9\times10^{-7}$ s^{-1}. The variance spectrum of simulated isotropic turbulent flow (black curves) with the same parameters as in Figure 4 is plotted for comparison.

$$\xi_2=\nabla^2\psi_2-S_2(\psi_2-\psi_1)$$

The stratification parameters define the first baroclinic Rossby deformation radius $R_d=\frac{1}{\sqrt{S_1+S_2}}$, which serves as the energy injection length scale. The Rossby deformation radius is 25 km.

Isotropic turbulence simulations were conducted on the *f*-plane

$$\frac{\partial\xi_1}{\partial t}+J(\psi_1,\xi_1)=F+\nu\nabla^4\psi_1 \tag{5}$$

$$\frac{\partial\xi_2}{\partial t}+J(\psi_2,\xi_2)=-\gamma\nabla^2\psi_2+\nu\nabla^4\psi_2 \tag{6}$$

with a forcing function of the following form:

$$F(x,y,t)=Re\left(\sum_{m=1}^{N_x}\sum_{n=1}^{N_y}\left(A\frac{1}{\sqrt{\delta t}}w_{mn}e^{i\phi(t)}\right)e^{i(k_m x+\mathrm{l_n}y)}\right)$$

where A is a constant amplitude, $\sqrt{\delta t}$ is a square root of the time step, $\phi(t)$ is a randomly chosen phase from the interval $[0,2\pi]$ of a uniform distribution, $k_m=\frac{m}{L_x}$ and $\mathrm{l_n}=\frac{n}{L_y}$ are the wave numbers in the zonal and

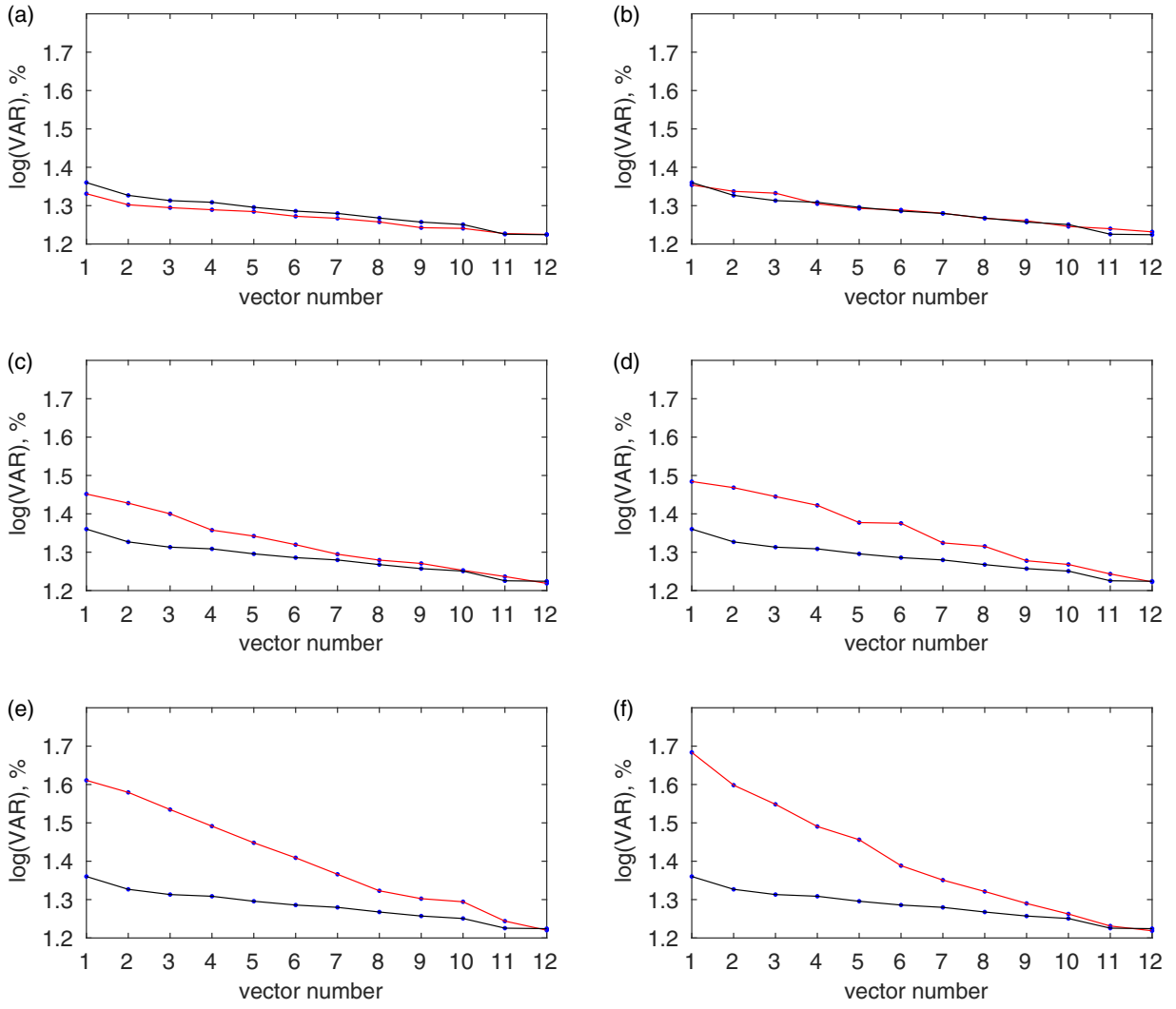

Figure 9. Amount of explained variance by 12 leading EOF modes of simulated anisotropic turbulent flow (red curves) for $\gamma=5\times10^{-7}$ s^{-1} and (a) $\beta=1.14\times10^{-11}$ m^{-1} s^{-1}, (b) $\beta=1.47\times10^{-11}$ m^{-1} s^{-1}, (c) $\beta=1.75\times10^{-11}$ m^{-1} s^{-1}, (d) $\beta=1.98\times10^{-11}$ m^{-1} s^{-1}, (e) $\beta=2.15\times10^{-11}$ m^{-1} s^{-1}, and (f) $\beta=2.25\times10^{-11}$ m^{-1} s^{-1}. The variance spectrum of simulated isotropic turbulent flow (black curves) with the same parameters as in Figure 4 is plotted for comparison.

meridional directions, and L_x and L_y are the length of the domain in the zonal and meridional directions. We use the "ring-shaped" forcing function for which

$$w_{mn}=\begin{cases}1, & |K-K_f|\le 3\\ 0, & |K-K_f|>3.\end{cases} \tag{7}$$

$K=\sqrt{k_m^2+l_n^2}$, $K_f=33$. This is a typical forcing function used in many studies of two-dimensional turbulence (Danilov & Gurarie, 2000).

The model was integrated over the rectangular domain ($L_x\times L_y$, $L_y=3,600$ km and $L_x=7,200$ km) and over the square domain ($L_x\times L_y$, $L_x=3,600$ km and $L_y=3,600$ km). The number of grid points in the zonal and meridional directions was chosen to be $N_x=512$ and $N_y=256$ for the rectangular domain, and $N_x=N_y=256$ for the square domain. This gives a resolution of approximately 14 km for both cases. Periodic boundary conditions were applied on each boundary. The nonlinear terms were discretized with the Arakawa energy, enstrophy, and symmetry conserving scheme (Arakawa, 1966). Time integration was performed with Adams-Bashford third-order scheme for 70,000 days, or equivalently, 192 years.

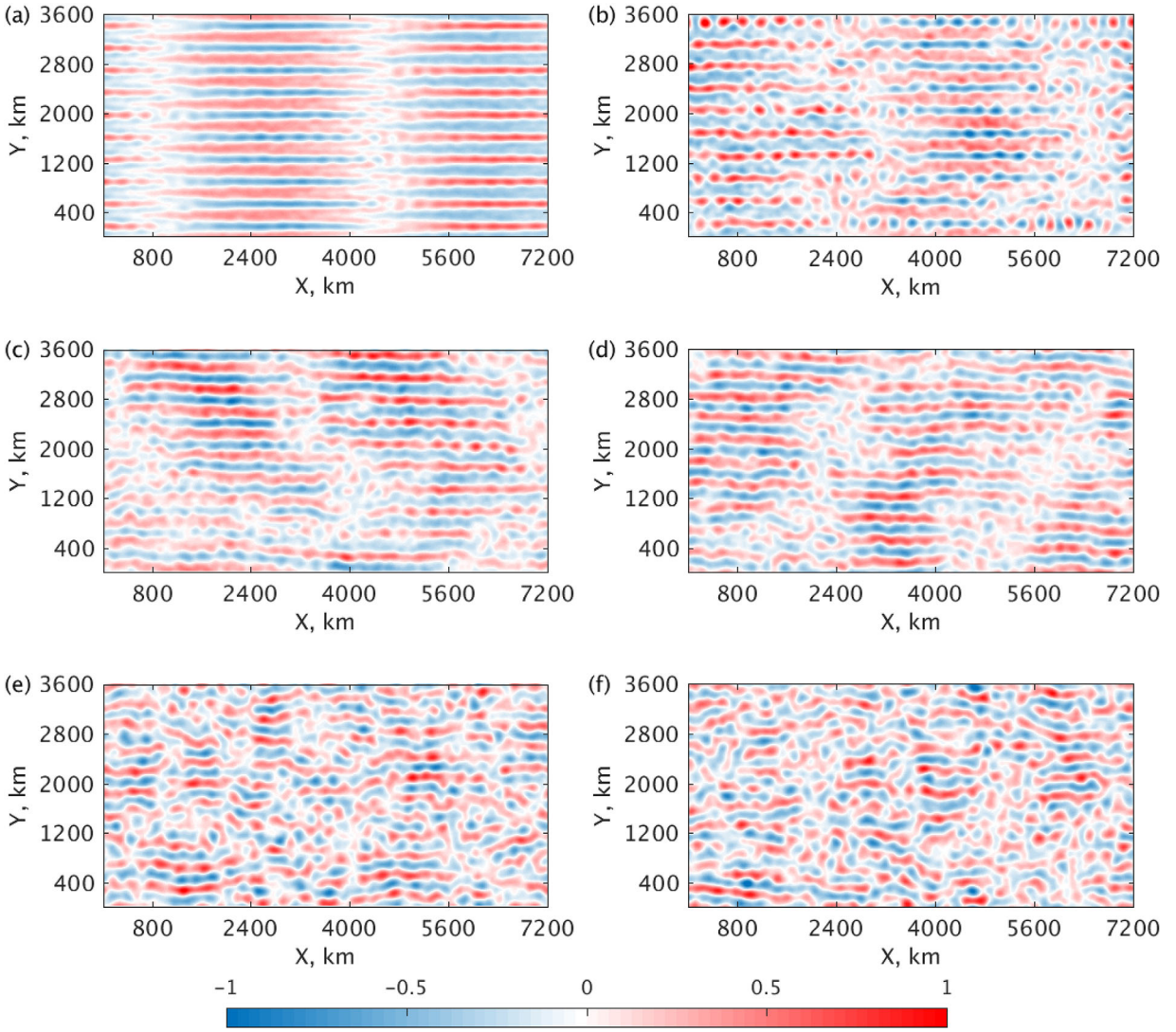

Figure 10. EOF1×10^{-3} of simulated anisotropic turbulent flow for β=2.15×10^{-11} m^{-1} s^{-1} and (a) γ=1×10^{-7} s^{-1}, (b) γ=2×10^{-7} s^{-1}, (c) γ=3×10^{-7} s^{-1}, (d) γ=4×10^{-7} s^{-1}, (e) γ=7×10^{-7} s^{-1}, and (f) γ=9×10^{-7} s^{-1}.

Examples of model output are shown in Figure 1. Simulated anisotropic turbulent flow (Figure 1a) consists of multiple zonal jets and numerous eddies. Isotropic turbulent flow contains eddies propagating around the domain and interacting with each other (Figure 1b). Unlike the anisotropic turbulent flow, the isotropic flow does not have a preference for zonal direction and is not expected to have ZELTs.

3. Phenomenology

3.1. Separating ZELTs From the Background Field

In this section, we perform simulations of anisotropic (γ=3×10^{-7} s^{-1}, β=2.15×10^{-11} m^{-1} s^{-1}) and isotropic (γ=3×10^{-7} s^{-1}, β=0×10^{-11} m^{-1} s^{-1}) turbulent flows and utilize them as a test bed for the efficiency of EOF versus Fourier decompositions in extracting ZELTs from the background flow. The simulations are performed on a square domain for the ease of comparison. To unambiguously distinguish ZELTs from previously analyzed zonal jets (Berloff et al., 2011 and all references therein; see also Venaille et al., 2014), we remove the zonal and time-mean component of the total flow.

The spatial Fourier spectrum of the velocity stream function for anisotropic turbulence simulation shows a power peak located at long zonal wavelengths and outlined by a rectangle (Figure 2a). Isolating spectral

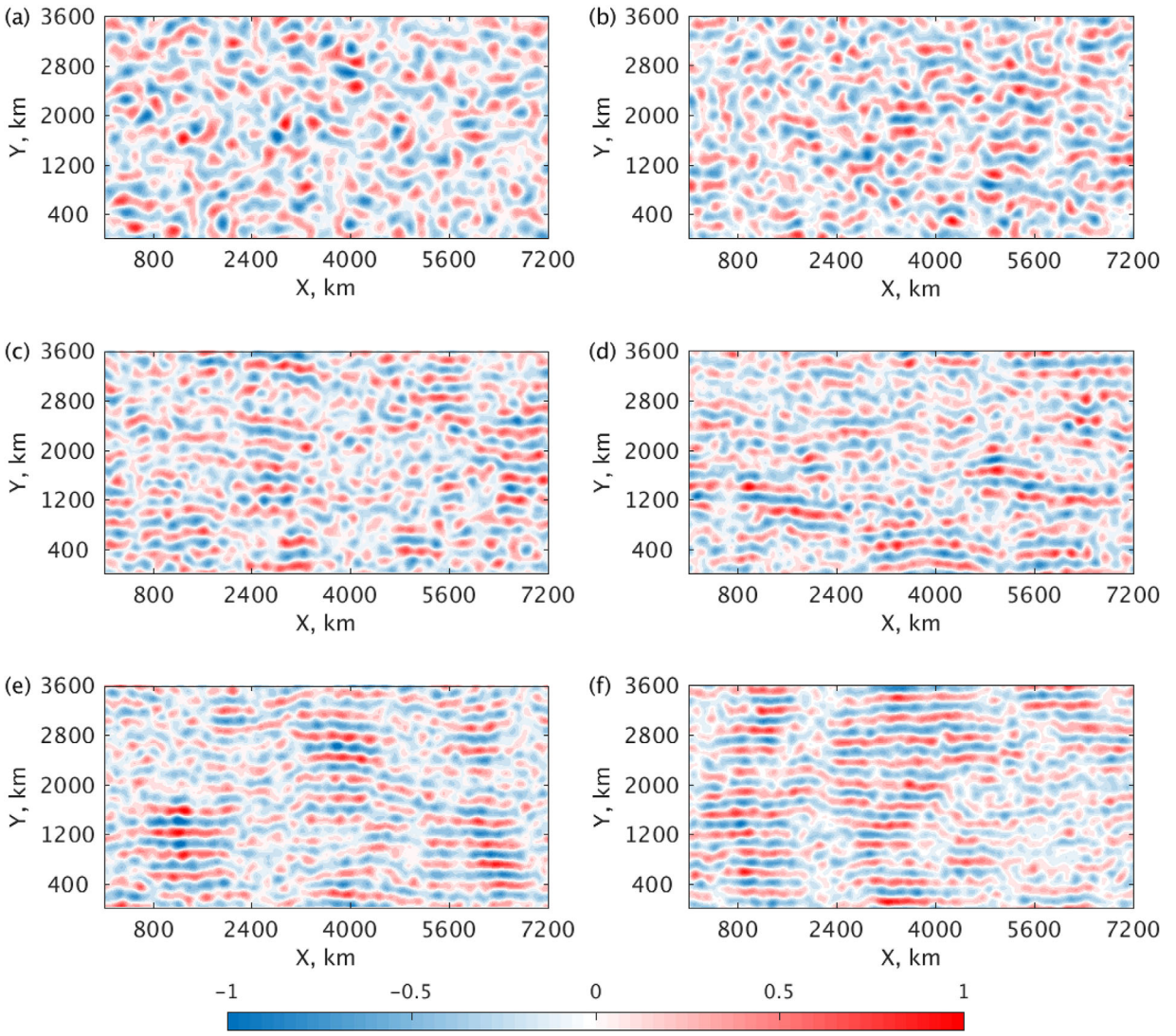

Figure 11. EOF1$\times 10^{-3}$ of simulated anisotropic turbulent flow for $\gamma=5\times10^{-7}$ s^{-1} and (a) $\beta=1.14\times10^{-11}$ m^{-1} s^{-1}, (b) $\beta=1.47\times10^{-11}$ m^{-1} s^{-1}, (c) $\beta=1.75\times10^{-11}$ m^{-1} s^{-1}, (d) $\beta=1.98\times10^{-11}$ m^{-1} s^{-1}, (e) $\beta=2.15\times10^{-11}$ m^{-1} s^{-1}, and (f) $\beta=2.25\times10^{-11}$ m^{-1} s^{-1}.

modes corresponding to this power peak we readily obtain zonally elongated flow patterns, which can be associated with ZELTs (Figure 3a). Two major problems arise with this approach of identifying ZELTs. First, the cut-off wave numbers are not unique; we choose these wave numbers rather subjectively (1 and 3 along *k*-axis, and 8 and 12 along *l*-axis). Second, spatial Fourier filtering can produce bogus flow patterns. To illustrate this point, we apply the same Fourier filter to simulated isotropic turbulent flow with its spectrum shown in Figure 2b. Since ZELTs do not exist in such a flow, the extracted zonally elongated flow patterns (Figure 3b) are clearly the artifact of the filtering procedure. Unlike Fourier decomposition, EOF decomposition does not suffer these shortcomings. We next test the efficiency of the filter based on EOF decomposition (see also Chen et al., 2016). The technical details are presented in Appendix A.

Comparing the amount of the explained variance by each of the EOF modes, one can see that the variance spectrum of the anisotropic turbulence is steeper than one of the isotropic turbulence (Figure 4). While the EOF modes of the isotropic turbulent flow are not well-separated, the first four EOF modes of anisotropic turbulent flow are clearly distinct from the rest of the spectrum. This is further confirmed by the spatial structure of the first four EOFs displayed in Figure 5a. Unlike higher order EOFs that do not exhibit long zonal length scales (not shown), these four leading modes have the form of zonally extended patterns with several eddies superimposed on them (see also Ivanov et al., 2012). This spatial structure is also in sharp

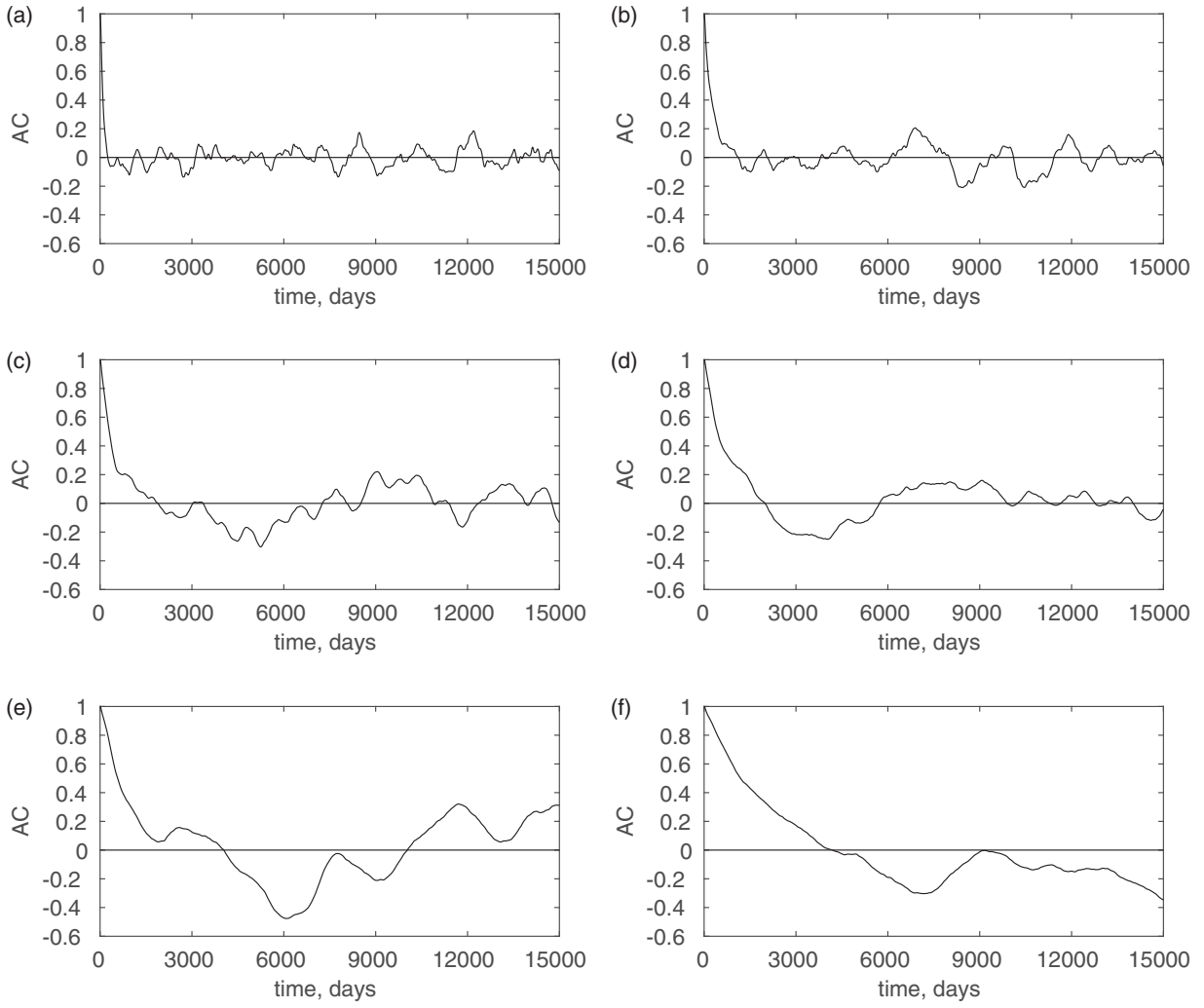

Figure 12. ACF of PC1 of simulated anisotropic turbulent flow for β=2.15×10^{-11} m^{-1} s^{-1} and (a) γ=1×10^{-7} s^{-1}, (b) γ=2×10^{-7} s^{-1}, (c) γ=3×10^{-7} s^{-1}, (d) γ=4×10^{-7} s^{-1}, (e) γ=7×10^{-7} s^{-1}, and (f) γ=9×10^{-7} s^{-1}.

contrast to EOFs of the isotropic turbulent flow, which display randomly distributed eddies (Figure 5b). The autocorrelation function (ACF) of the corresponding Principal Components (PC) oscillates and decays slowly for all four leading EOFs of the anisotropic turbulent flow (Figure 6a). This is at odds with the four leading EOFs of isotropic turbulent flow, for which the ACF of the corresponding PC decays quickly and fluctuates around zero.

In the rest of the study, we associate ZELTs with zonally elongated modes of flow variability. A convenient measure to quantify anisotropy of the flow field is the anisotropic ratio defined as $\alpha = \frac{<u'^2> - <v'^2>}{<u'^2> + <v'^2>}$, where $< >$ denotes spatial averaging, u' and v' are the zonal and meridional eddy velocities, respectively. Its values range from -1, for which the velocities are purely meridional, to 1, for which velocities are purely zonal. The value of $\alpha = 0$ indicates that the flow field is perfectly isotropic. We use this parameter to define the number of EOFs that represent ZELTs as those with anisotropic ratio $\alpha \geq 0.6$. In the case discussed above, only four EOF modes have anisotropic ratio $\alpha \geq 0.6$.

3.2. Propagation of ZELTs

One important property of a distinct flow structure is its ability to propagate across the medium. By construction, each separate EOF mode can be interpreted as a stationary oscillation, so the propagation of the flow structure it represents cannot be tracked. Unlike regular EOF decomposition, which makes use only of

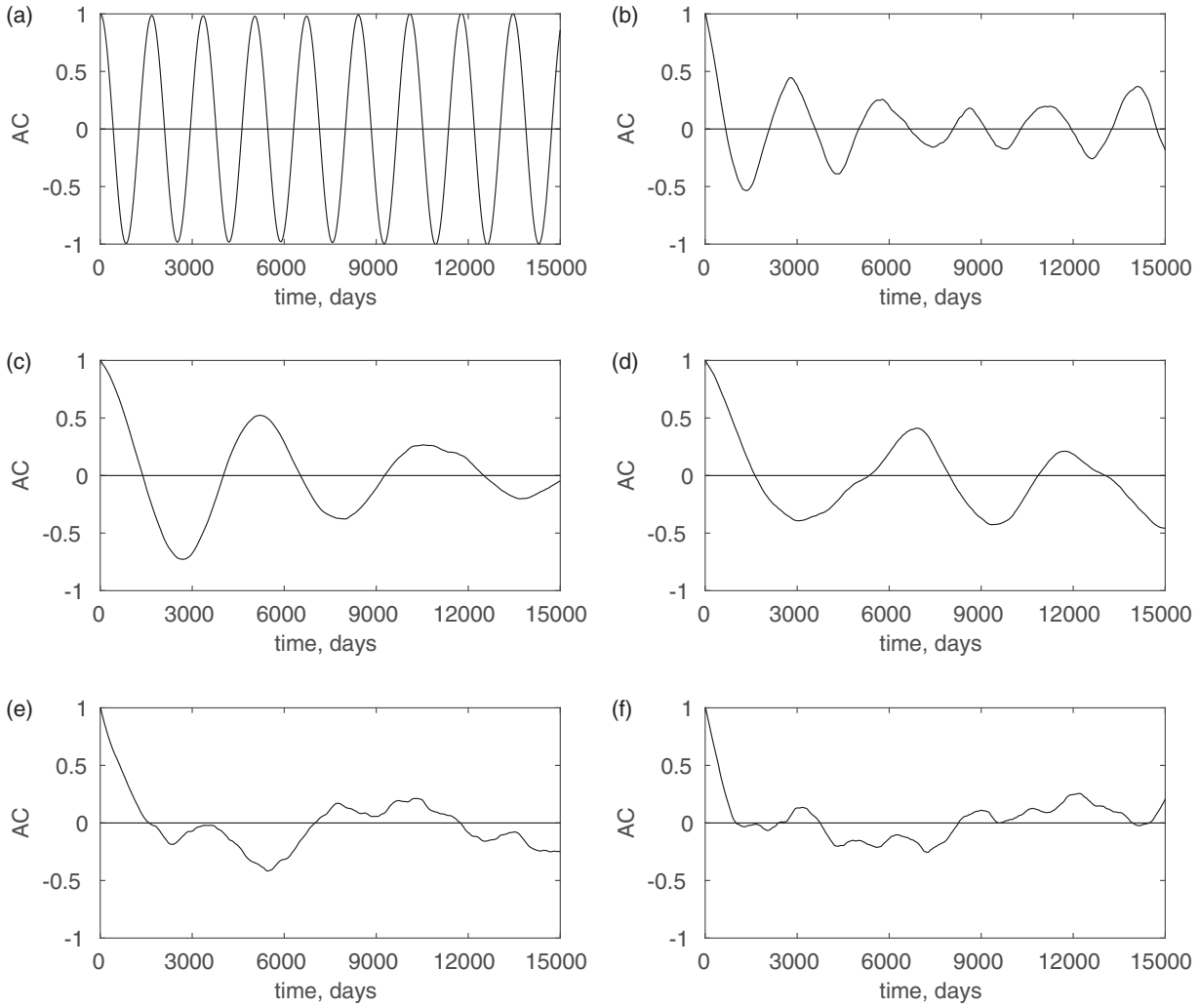

Figure 13. ACF of PC1 of simulated anisotropic turbulent flow for $\gamma=5\times10^{-7}$ s^{-1} and (a) $\beta=1.14\times10^{-11}$ m^{-1} s^{-1}, (b) $\beta=1.47\times10^{-11}$ m^{-1} s^{-1}, (c) $\beta=1.75\times10^{-11}$ m^{-1} s^{-1}, (d) $\beta=1.98\times10^{-11}$ m^{-1} s^{-1}, (e) $\beta=2.15\times10^{-11}$ m^{-1} s^{-1}, and (f) $\beta=2.25\times10^{-11}$ m^{-1} s^{-1}.

spatial correlation of the data set, Extended EOF decomposition also takes into account the fact that geophysical data are usually highly correlated in time. This allows us to track the propagation of ZELTs and estimate their speed.

Figure 7 shows the zonal-time and meridional-time Hovmöller diagrams of the Extended EOF1. The spatial structure of these Extended EOFs closely matches the regular EOFs discussed earlier and is not shown here. Due to computational expense required to compute Extended EOFs, we use only three time lags: 500, 1,000, and 1,500 days. As indicated by slanted contours in the zonal-time diagram (Figure 7a), the signal propagates westward with the speed of around 1.15 cm s^{-1}. Nearly vertical contours in the meridional-time diagram (Figure 7b) suggest that ZELTs have negligible meridional speed. The zonal propagation speed can be compared to the zonal phase speed of linear modes for the Phillips model, which gives 4.75–5 cm s^{-1} for small zonal wave numbers (see formula 7.11.6 in Pedlosky, 2013). Higher order Extended EOFs, which are involved in representing ZELTs, show similar slopes in the zonal-time and meridional-time Hovmöller diagrams.

The discrepancy between the values of propagation speed suggests that ZELTs are nonlinear phenomenon and cannot be explained by linear dynamics. However, Berloff and Kamenkovich (2013a, 2013b) demonstrate that accounting for modulations of the mean flow by stationary zonal jets can alter the propagation of linear modes and result in close match between nonlinear and linear dynamics.

4. Sensitivity Analysis

4.1. Sensitivity to a Single Parameter

In this section, we examine the sensitivity of ZELTs properties to two model parameters, planetary vorticity gradient β and bottom friction γ. Sensitivity to other model parameters, such as vertical stratification and lateral friction, is found to be weak and is not discussed in this section. We first study the sensitivity to each of these parameters separately, by fixing one parameter and varying the other. The corresponding values are given in Table 1.

Variance spectra are shown in Figure 8 (varying γ, fixed β) and Figure 9 (varying β, fixed γ). The variance spectrum of isotropic turbulence also shown in these plots is identical to the one in Figure 4. The general property of the spectra is that for larger values of γ and smaller values of β, the flatter the spectrum tends to be. For $\gamma=9\times10^{-7}\,s^{-1}$ and $\beta=1.14\times10^{-11}\,m^{-1}\,s^{-1}$, the spectra of the isotropic and anisotropic turbulence are nearly identical. The regime at low values of bottom friction is unusual. First, for the case of fixed $\beta=2.15\times10^{-11}\,m^{-1}\ s^{-1}$ and $\gamma=1\times10^{-7}\,s^{-1}$, only two EOF modes are strongly separated from the rest of the spectrum (Figure 8a). Second, there is a substantial decrease in the amount of the explained variance by the leading EOFs between the cases of $\gamma=1\times10^{-7}\,s^{-1}$ and $\gamma=2\times10^{-7}\,s^{-1}$ (Figures 8a and 8b).

We next discuss the sensitivity of the spatial structure of ZELTs. Even though ZELTs are represented as several leading EOFs (Table 1), the changes in ZELT structure can be derived from analyzing only the first mode (EOF1). For some parameters, there are no EOFs with anisotropic ratio $\alpha \geq 0.6$ (Table 1). However, this value was chosen rather arbitrarily and, as we will see below, some leading EOFs are still characterized by a rather noticeable degree of anisotropy. The changes in EOF1 confirms the expectation from the analysis of the variance spectrum: EOF1 becomes more isotropic with increasing bottom drag γ (Figure 10) and decreasing β (Figure 11). EOF1 remains anisotropic even for very large values of γ ($\gamma=9\times10^{-7}\,s^{-1}$), whereas no signature of zonal anisotropy is observed for small values of β ($\beta=1.14\times10^{-11}\,m^{-1}\,s^{-1}$). The sharp transition in the shape of the variance spectra between $\gamma=1\times10^{-7}\,s^{-1}$ and $\gamma=2\times10^{-7}\,s^{-1}$ is also reflected in the spatial

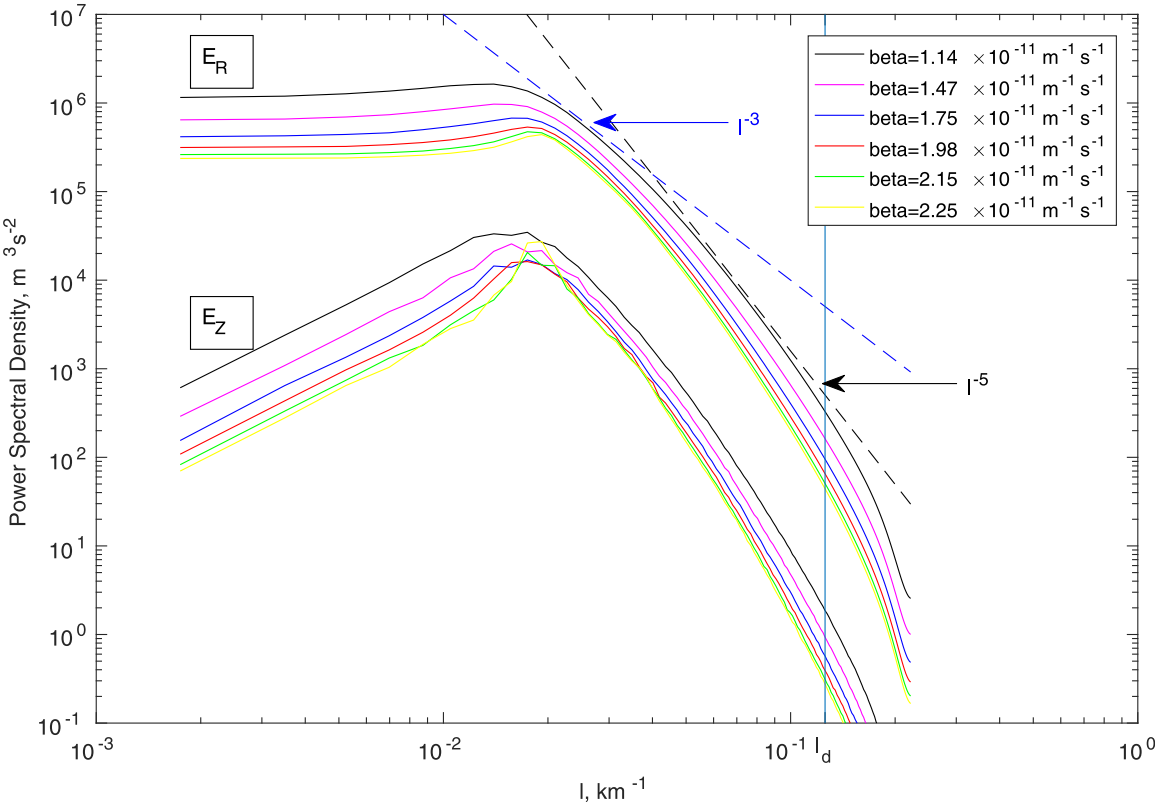

Figure 14. Zonal (E_Z) and residual (E_R) spectra of barotropic kinetic energy for $\beta=2.15\times10^{-11}\,m^{-1}\ s^{-1}$ and varying γ. The vertical line denotes meridional wave number for Rossby deformation radius (l_d).

structure of EOF1, which changes from strictly structured, nearly zonal patterns to meandering bands with eddies embedded in them. We also quantify baroclinicity of ZELTs by computing the root mean square of the ratio between barotropic and baroclinic components of EOF1 (Table 1); the results suggest that EOF1 has a stronger baroclinic component except for $\gamma=1\times10^{-7}\,s^{-1}$ case, in which the magnitude of baroclinic and barotropic components are nearly identical.

The impact of environmental parameters on the temporal variability of ZELTs can be deduced from changes in the ACF of PC1 structure, which for the cases with fixed $\beta=2.15\times10^{-11}\,m^{-1}\,s^{-1}$ shows that the leading mode of variability exhibits perfect oscillations for low values of bottom friction ($\gamma=1\times10^{-7}\,s^{-1}$), damped oscillations for the moderate values ($\gamma=2\times10^{-7}\,s^{-1}, 3\times10^{-7}\,s^{-1}, 4\times10^{-7}\,s^{-1}$) and a noisy decay modulated by wiggles for the high values ($\gamma=7\times10^{-7}\,s^{-1}, 9\times10^{-7}\,s^{-1}$) (Figure 12). For the cases of fixed γ, the ACF of PC1 is characterized only by decaying behavior, and the decay occurs faster with decreasing β (Figure 13). This is evidenced by a decreasing decorrelation time scale, defined here and elsewhere as a time lag of the first zero crossing of ACF. When β reaches its minimum value $1.14\times10^{-11}\,m^{-1}\,s^{-1}$, the decorrelation time scale becomes very short and the ACF of PC1 bears a lot of resemblance to the one of the isotropic turbulence simulation.

Lastly, we compare the energy spectra of simulated baroclinic and barotropic turbullent flows. Two distinct regimes can be found in simulations of barotropic turbulence on the β-plane: zonostrophic regime, in which turbulence develops strong anisotropy with -5 (zonal spectrum) and $-\frac{5}{3}$ (residual spectrum) slopes of energy spectra and friction-dominated regime featuring $-\frac{8}{3}$ (zonal spectrum) and $-\frac{5}{3}$ (residual spectrum) slopes of energy spectra analogous to classical isotropic turbulence (Galperin et al., 2010; Sukoriansky et al., 2007). In contrast, our simulations demonstrate that both zonal and residual spectra have rather steep slope close to -5 for all considered parameter values (Figures 14 and 15; but see also Berloff & Kamenkovich (2013b)). Such an unexpected steepness of energy spectra and the potential role of ZELTs in causing it certainly require further investigation.

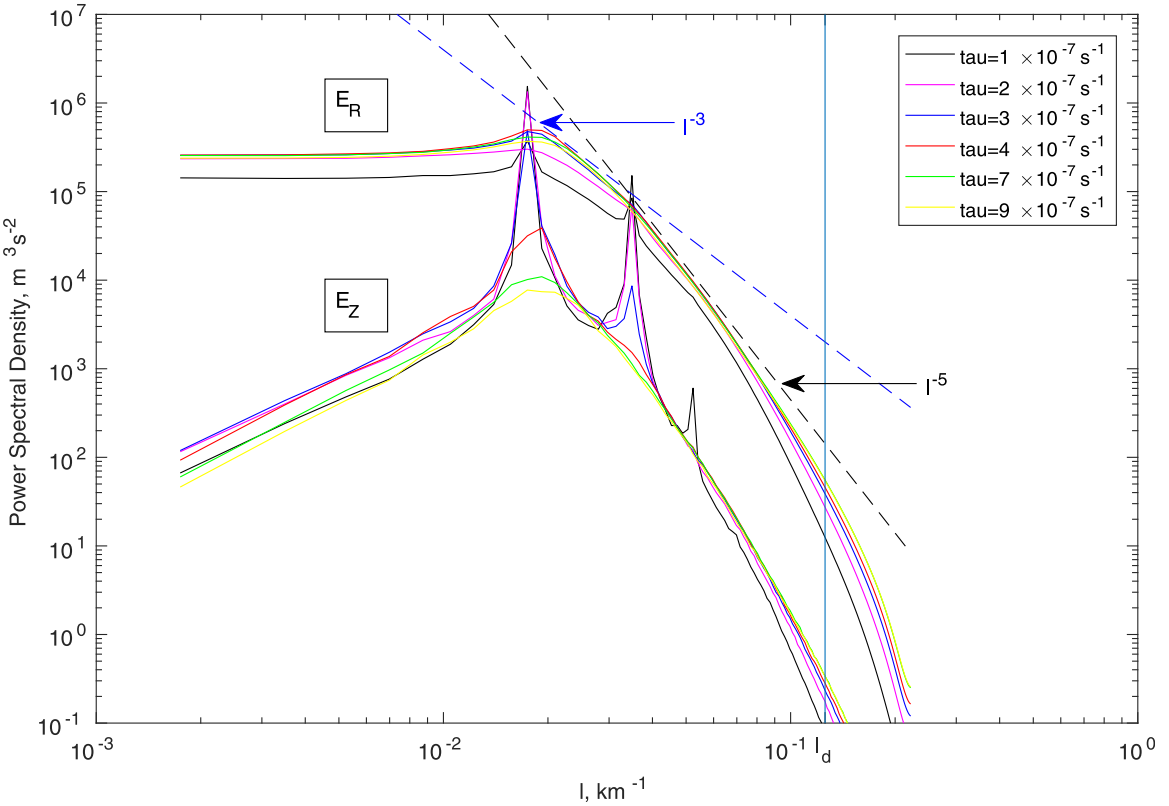

Figure 15. Zonal (E_Z) and residual (E_R) spectra of barotropic kinetic energy for $\gamma=5\times10^{-7}\,s^{-1}$ and varying β. The vertical line denotes meridional wave number for Rossby deformation radius (l_d).

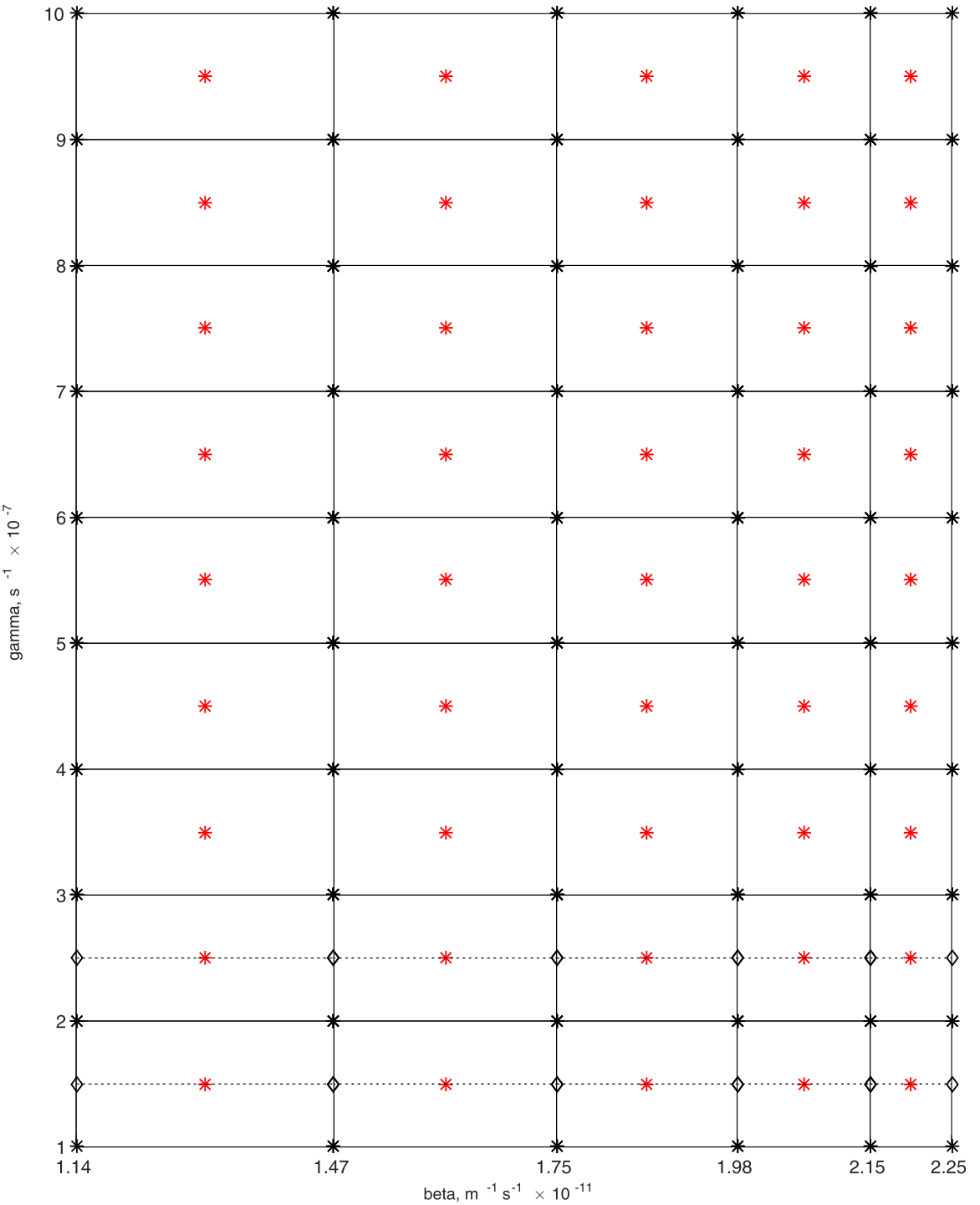

Figure 16. Interpolation points in $\beta - \gamma$ parameter space (black $*$); diamonds ($\diamond$) are additional interpolation points; red $*$ are the points at which the response surface is validated.

4.2. Joint Sensitivity Analysis

In the previous subsection, we showed that for some parameter values the EOF1 apparently lacks zonal anisotropy. In this section, we investigate anisotropy of EOF1 by constructing the response surface, which shows the changes in the anisotropic ratio α due to simultaneous variations in γ and β. Being a nonquadratic quantity, the anisotropic ratio cannot be easily split into contributions from several EOFs. We construct the response surface for EOF1 only and associate the changes in it with the changes in ZELTs. The

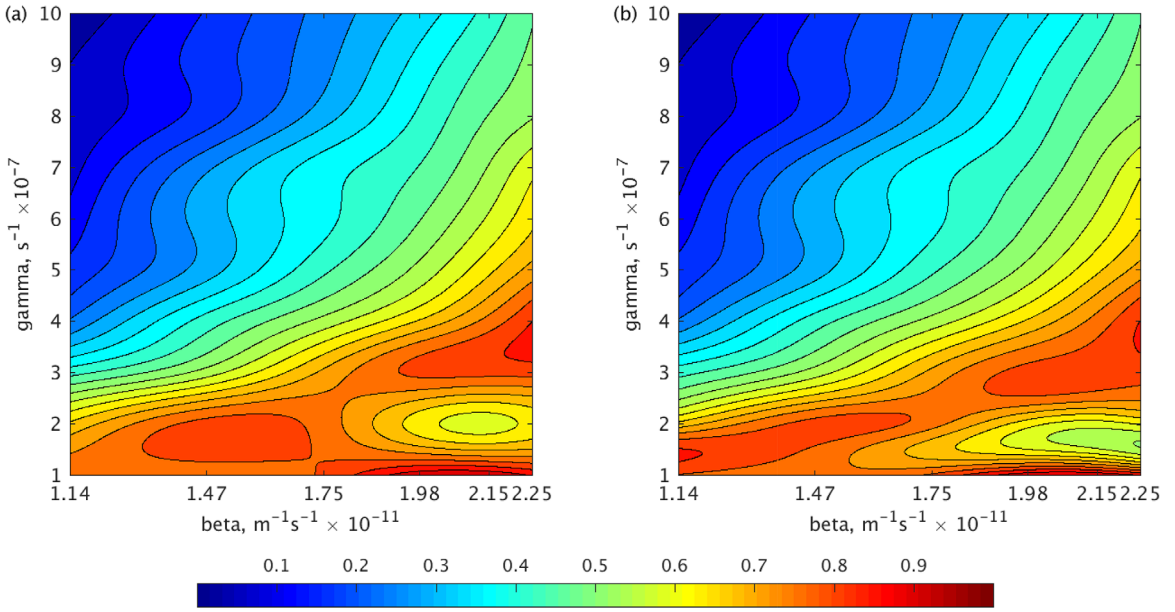

Figure 17. Response surface of anisotropic ratio derived from the EOF1 for smoothing parameter $p = 0.5$. The surfaces obtained (a) without and (b) with additional interpolation points.

response surfaces of several higher order leading EOFs do not provide any additional information. The technical details of the response surface construction are presented in Appendix B.

The anisotropic ratio is <0.2 in the upper-left corner of the response surface, indicating that the leading EOF is nearly isotropic and ZELTs do not exist in that region of the parameter space (Figure 17b). Increasing from the upper-left to the lower-right corner along the diagonal, the anisotropic ratio goes through intermediate values (0.3–0.7) and reaches high values ($\sim$0.8). We associate the values of $\alpha \geq 0.6$ with ZELTs being present in the flow field and identify the swath of the $\alpha \sim 0.8$ as the region, in which ZELTs are the

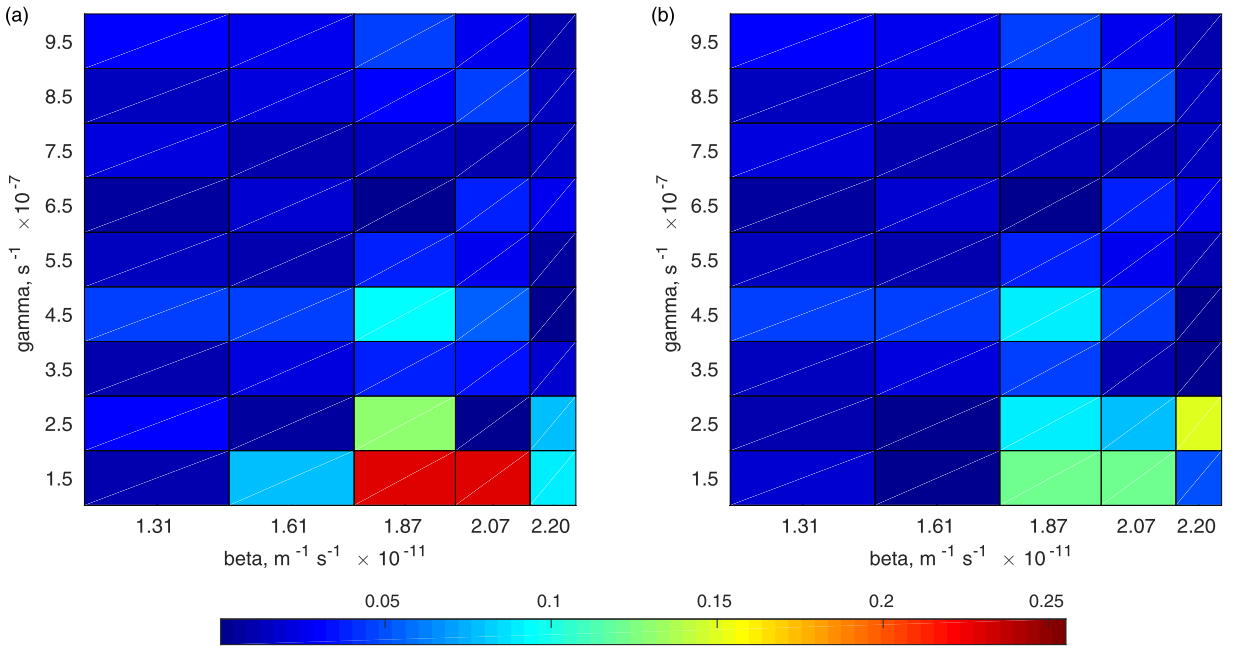

Figure 18. Validation error of the response surface for smoothing parameter $p = 0.5$. The error computed for response surfaces (a) without and (b) with additional interpolation points.

most pronounced. Another swath with $\alpha \sim 0.9$ indicates that EOF1 is strongly anisotropic analogous to the one seen in Figure 10a. These two swathes are separated by the tongue of moderate values of $\alpha \simeq 0.5$, the origin of which remains unclear. We were not able to run the numerical model for $\gamma < 1\times10^{-7}\,s^{-1}$ and small values of β. This limits the considered parameter space.

Finally, we compare the sensitivity of the anisotropic ratio α in our model with the geographical distribution of α estimated from observations in Scott et al. (2008). The highest values of α in Figure 4 of Scott et al. (2008) are 0.5–0.6 and are found at around 20°S–30°S, decreasing poleward up to 0.3–0.4 between 30°S and 40°S and reaching the minimum values of ~0.1 at 30°S–60°S, although some spots of large values of α are also observed. The range of values of bottom drag γ in the real ocean is largely unknown. However, taking this value to be equal to $5\times10^{-7}\,s^{-1}$ we readily observe the consistency between the prediction of idealized model and observations. We also note that the values of anisotropic ratio computed from altimetry data never reach the values higher than 0.6. This can be explained by the fact that the intensity of the signal associated with ZELTs in the real ocean can be weakened by other types of mesoscale variability not included in our idealized model.

5. Discussion and Conclusions

This study demonstrates that ZELTs represent the leading mode of mesoscale variability in baroclinic turbulent flow and have properties and structure that are sensitive several environmental factors. We test the performance of two filtering techniques to efficiently separate ZELTs from the background flow and quantify the sensitivity of ZELTs properties to changes in the bottom drag coefficient and the meridional gradient of planetary vorticity.

Low pass Fourier filtered isotropic and anisotropic turbulent flow fields reveal a series of similar zonally elongated patterns, thereby suggesting the inadequacy of this technique to identify ZELTs. Alternatively, the EOF decomposition provides a framework for efficient representation of ZELTs. The leading EOF modes derived from the anisotropic turbulent flow field reveal a series of zonally elongated patterns with eddies embedded in them, while each EOF mode of an isotropic turbulent flow field consists of randomly distributed eddies. The variance spectrum of anisotropic turbulent flow is steeper with several leading EOFS being well-separated from the remaining EOFs. Analyzing the ACF of the corresponding PCs, we found that it oscillates with a slow decay for the anisotropic turbulent flow and fluctuates around zero followed by a fast decay for the isotropic turbulent flow. We also investigated the propagation of ZELTs by means of Extended EOF decomposition. As revealed by Hovfmöller diagrams of the leading Extended EOF, the patterns propagate in the zonal direction.

The spatiotemporal variability of ZELTs is strongly affected by bottom drag (γ) and the meridional gradient of planetary vorticity (β). Decreasing β or increasing γ each leads to flattening of the variance spectra, isotropization of the EOF1 and faster decay of ACF of PC1. The response surface of the anisotropic ratio reveals the region of relatively high values (~0.8) in the $\beta - \gamma$ parameter space; ZELTs are the most pronounced in this region.

This study suggests that the mesoscale variability at low-latitude and midlatitude can be dominated by zonally propagating ZELTs. As a consequence, any attempts to parameterize the impact of mesoscale eddies by the isotropic viscosity and diffusivity will lead to biases in simulated flow and tracer distribution (see Kamenkovich et al., 2015, for example). The results reported in this paper reveal complicated phenomenological and structural properties of ZELTs, with the underpinning mechanism of their formation and maintenance remaining unknown. This will be a subject of a separate study.

Appendix A: Computational Aspects of EOF/EEOF

We discuss some of the key properties of Empirical Orthogonal Functions (EOF) and Extended Empirical Orthogonal Functions (EEOF), and present the technical details of their computation pertinent to our model configuration. For general discussion of EOF application to turbulent flows, the reader can consult Berkooz et al. (1993), Holmes (2012), Aubry et al. (1988), and Sirovich (1987a, 1987b).

The output of the model is represented as a two-dimensional matrix $\mathbf{X}_{ml}$, where index m corresponds to a grid point and index l denotes sampling time, $m=1,\ldots,N_{gr}$, $l=1,\ldots,T$. Here N_{gr} is the number of grid points of the computational domain, T is the number of samples. Each column of this matrix is a state vector at a particular instance, which is assumed to have zero time mean. The matrix is a discrete version of time-evolving, continuous state vector $\mathbf{x}(t)$. The computation of EOFs boils down to the eigenvalue problem

$$\mathbf{A}_{mm}\phi_m=\lambda_m\phi_m \tag{A1}$$

where λ_m are the eigenvalues and ϕ_m are the corresponding eigenvectors (EOF). A_{mm} is a covariance matrix defined as

$$\mathbf{A}_{mm}=\sum_{l=1}^{T}\mathbf{X}_{ml}\mathbf{X}_{lm} \tag{A2}$$

Direct computation of eigenvectors and eigenvalues of matrix A_{mm} is impossible due to the enormous size of the matrix. To circumvent this problem, we instead compute the eigenvectors and eigenvalues of matrix $\mathbf{B}_{ll}=\sum_{m=1}^{N_{gr}}\mathbf{X}_{lm}\mathbf{X}_{ml}$, which has the same nonzero eigenvalues as matrix $\mathbf{A}_{mm}$ and its eigenvectors related to the eigenvectors η_l of matrix $\mathbf{B}_{ll}$ through a simple linear transformation (Von Storch & Zwiers, 2002)

$$\phi_m=\sum_{l=1}^{T}\frac{X_{ml}}{det(X_{ml})}\eta_l$$

Since the covariance matrix $\mathbf{A}_{mm}$ is positive definite, the eigenvectors (EOF) of this matrix form a complete orthonormal basis in the space with appropriately chosen inner product. Examples of the inner product include area integrated energy, enstrophy, or squared stream function. Since the focus of this study is on large-scale flows, we use the inner product in the form of squared stream function (Selten, 1995). Now, the state vector $\mathbf{x}(t)$, that is stream function, can be expanded in series over this basis

$$\mathbf{x}(t)=\sum_{k=1}^{T}\alpha_k(t)\phi_k \tag{A3}$$

where the expansion coefficients $\alpha_k(t)$ are referred to as Principal Components (PC). The basis spanned by EOF suggest that the squared norm generated by the inner product, or equivalently the variance, is minimized. The EOFs are typically arranged according to the fraction of explained variance, which can be expressed as

$$\frac{var(x_k)}{\sum_{i=1}^{T}var\ x_i}=\frac{\lambda_k}{\sum_{i=1}^{T}\lambda_i} \tag{A4}$$

where $varx_k$ are variance of the kth EOF mode.

For Extended EOFs, the data matrix takes into account the correlation in time, so that index m runs as $m=1,\ldots,M*N_{gr}$, and index l runs as $l=1,\ldots,T-M+1$. Here M is a number of time lags. For the rest, Extended and regular EOFs are computed in a similar fashion.

Appendix B: Response Surface Construction

We introduce the basic idea of the response surface construction (Iskandarani et al., 2016). For simplicity, consider anisotropic ratio α, which depends only on a single parameter γ. The $\tilde{\alpha}(\gamma)$ approximates the true anisotropic ratio $\alpha(\gamma)$ computed at several points in the parameter space and can be represented as a series expansion over some basis:

$$\alpha(\gamma)=\tilde{\alpha}(\gamma)+\epsilon(\gamma)=\sum_{i=1}^{M+3}c_i\phi_i(\gamma)+\epsilon(\gamma) \tag{B1}$$

where ϵ is an error committed by the approximation, $\phi_i(\gamma)$ are the basis functions, and c_i are the expansion coefficients to be determined. In this study, we choose $\phi_i(\gamma)$ in the form of cubic B-splines (Chin et al., 2004; De Boor, 1978; Inoue, 1986)

$$\phi_i(\gamma)=\begin{cases}0, & \gamma<\xi_{i-4}\\ B_1\left(\frac{\gamma-\xi_{i-4}}{f}\right), & \xi_{i-4}<\gamma<\xi_{i-3}\\ B_2\left(\frac{\gamma-\xi_{i-3}}{f}\right), & \xi_{i-3}<\gamma<\xi_{i-2}\\ B_3\left(\frac{\gamma-\xi_{i-2}}{f}\right), & \xi_{i-2}<\gamma<\xi_{i-1}\\ B_4\left(\frac{\gamma-\xi_{i-1}}{f}\right), & \xi_{i-1}<\gamma<\xi_i\\ 0, & \xi_i<\gamma.\end{cases} \tag{B2}$$

where $\xi_{-3}\ldots\xi_0,\xi_1,\ldots,\xi_M\ldots\xi_{M+3}$ are equispaced knots, f is a common knot interval and

$$B_1(r)=\frac{r^3}{6}$$

$$B_2(r)=\frac{-3r^3+3r^2+3r+1}{6}$$

$$B_3(r)=\frac{3r^3-6r^2+4}{6}$$

$$B_4(r)=\frac{-r^3+3r^2-3r+1}{6}$$

The coefficients c_i are determined by minimizing the error norm. We choose the norm in the following form:

$$||\epsilon(\gamma)||=p\sum_{i=1}^{M+3}\left(\frac{f(\gamma_i)-\tilde{f}(\gamma_i)}{\delta f(\gamma_i)}\right)^2+(1-p)\int_{\gamma_1}^{\gamma_M}f_\gamma^2 d\gamma \tag{B3}$$

Here $\alpha(\gamma_i)$ and $\tilde{\alpha}(\gamma_i)$ are the values of anisotropic ratio $\alpha(\gamma)$ and its approximation $\tilde{\alpha}(\gamma)$ at the data sites γ_i, $\delta\alpha(\gamma_i)$ is an estimate of the standard deviation in $\alpha(\gamma_i)$. The smoothing parameter p ranges from $p=0$, in which case the fit is just a straight line, to $p=1-$ the least-square fit. The generalization for multiple parameters case is straightforward. Now, our anisotropic ratio $\alpha(\gamma,\beta)$ depends on two parameters γ and β, and is approximated by $\tilde{\alpha}(\gamma,\beta)$ with committed error $\epsilon(\gamma,\beta)$

$$\alpha(\gamma,\beta)=\tilde{\alpha}(\gamma,\beta)+\epsilon(\gamma,\beta)=\sum_{i=1}^{M+3}\sum_{j=1}^{N+3}c_{ij}\phi_i(\gamma)\phi_i(\beta)+\epsilon(\gamma,\beta) \tag{B4}$$

and the coefficients c_{ij} are found by minimizing the error norm of the form

$$||\epsilon(\gamma,\beta)||=p\sum_{i=1}^{M+3}\sum_{j=1}^{N+3}\left(\frac{\alpha(\gamma_i,\beta_j)-\tilde{\alpha}(\gamma_i,\beta_j)}{\delta\alpha(\gamma_i,\beta_j)}\right)^2+(1-p)\int_{\gamma_1}^{\gamma_M}\int_{\beta_1}^{\beta_N}((\alpha_\gamma)^2+(\alpha_\beta)^2)d\beta d\gamma \tag{B5}$$

The values of data sites in the parameter space are shown in Figure 16 with black stars. The validation error is computed as

$$||\epsilon(\gamma_v,\beta_v)||=|\alpha(\gamma_v,\beta_v)-\tilde{\alpha}(\gamma_v,\beta_v)| \tag{B6}$$

The index v refers to the location of validation points in the parameter space marked by red stars in Figure 16.

Figure 17a displays the response surface obtained with interpolation points marked by black stars in Figure 16. Even though the value 0.5 of smoothing parameter gives the best approximation, the validation error shown in Figure 18a indicates that the surface approximates the anisotropic ratio poorly in the lower-right corner. After adding several interpolation points marked by diamonds as shown in Figure 16, the new response surface resolves more finer structures in the lower-right corner (Figure 17b) and the validation error is significantly decreased in that area (Figure 18b).

Acknowledgments
M.R. and I.K. are thankful to Dr. Pavel Berloff for some comments on this manuscript. M.R. and I.K. are supported by NSF grants OCE-0842834. Numerical model and data are available from https://doi.org/10.17604/M6HT03.

References

Arakawa, A. (1966). Computational design for long-term numerical integration of the equations of fluid motion: Two-dimensional incompressible flow. Part I. *Journal of Computational Physics*, *1*(1), 119–143.

Aubry, N., Holmes, P., Lumley, J. L., & Stone, E. (1988). The dynamics of coherent structures in the wall region of a turbulent boundary layer. *Journal of Fluid Mechanics*, *192*, 115–173.

Berkooz, G., Holmes, P., & Lumley, J. L. (1993). The proper orthogonal decomposition in the analysis of turbulent flows. *Annual Review of Fluid Mechanics*, *25*(1), 539–575.

Berloff, P., & Kamenkovich, I. (2013a). On spectral analysis of mesoscale eddies. Part I: Linear analysis. *Journal of Physical Oceanography*, *43*(12), 2505–2527.

Berloff, P., & Kamenkovich, I. (2013b). On spectral analysis of mesoscale eddies. Part II: Nonlinear analysis. *Journal of Physical Oceanography*, *43*(12), 2528–2544.

Berloff, P., Karabasov, S., Farrar, J. T., & Kamenkovich, I. (2011). On latency of multiple zonal jets in the oceans. *Journal of Fluid Mechanics*, *686*, 534–567.

Buckingham, C. E., & Cornillon, P. C. (2013). The contribution of eddies to striations in absolute dynamic topography. *Journal of Geophysical Research: Oceans*, *118*, 448–461. https://doi.org/10.1029/2012JC008231

Chen, C., Kamenkovich, I., & Berloff, P. (2016). Eddy trains and striations in quasigeostrophic simulations and the ocean. *Journal of Physical Oceanography*, *46*(9), 2807–2825.

Chin, T. M., Özgökmen, T. M., & Mariano, A. J. (2004). Multivariate-spline and scale-specific solution for variational analyses. *Journal of Atmospheric and Oceanic Technology*, *21*(2), 379–386.

Danilov, S. D., & Gurarie, D. (2000). Quasi-two-dimensional turbulence. *Physics-Uspekhi*, *43*(9), 863–900.

De Boor, C. (1978). *A practical guide to splines*. Berlin, Germany: Springer.

Galperin, B., Nakano, H., Huang, H.-P., & Sukoriansky, S. (2004). The ubiquitous zonal jets in the atmospheres of giant planets and earth's oceans. *Geophysical Research Letters*, *31*, L13303. https://doi.org/10.1029/2004GL019691

Galperin, B., Sukoriansky, S., & Dikovskaya, N. (2010). Geophysical flows with anisotropic turbulence and dispersive waves: Flows with a β-effect. *Ocean Dynamics*, *60*(2), 427–441.

Haidvogel, D. B., & Held, I. M. (1980). Homogeneous quasi-geostrophic turbulence driven by a uniform temperature gradient. *Journal of the Atmospheric Sciences*, *37*(12), 2644–2660.

Holmes, P. (2012). *Turbulence, coherent structures, dynamical systems and symmetry*. Cambridge, UK: Cambridge University Press.

Huang, H.-P., Kaplan, A., Curchitser, E. N., & Maximenko, N. A. (2007). The degree of anisotropy for mid-ocean currents from satellite observations and an eddy-permitting model simulation. *Journal of Geophysical Research*, *112*, C09005. https://doi.org/10.1029/2007JC004105

Inoue, H. (1986). A least-squares smooth fitting for irregularly spaced data: Finite-element approach using the cubic b-spline basis. *Geophysics*, *51*(11), 2051–2066.

Iskandarani, M., Wang, S., Srinivasan, A., Carlisle, T. W., Winokur, J., & Knio, O. M. (2016). An overview of uncertainty quantification techniques with application to oceanic and oil-spill simulations. *Journal of Geophysical Research: Oceans*, *121*, 2789–2808. https://doi.org/10.1002/2015JC011366

Ivanov, L. M., & Collins, C. A. (2009). *Modal decomposition of oceanic circulation: Applications for high-resolution models and Lagrangian data* (chap. 2, pp. 31–69). Hauppauge, NY: Nova Science Publishers.

Ivanov, L. M., Collins, C. A., & Margolina, T. M. (2012). Detection of oceanic quasi-zonal jets from altimetry observations. *Journal of Atmospheric and Oceanic Technology*, *29*(8), 1111–1126.

Kamenkovich, I., Rypina, I. I., & Berloff, P. (2015). Properties and origins of the anisotropic eddy-induced transport in the North Atlantic. *Journal of Physical Oceanography*, *45*(3), 778–791.

Laurindo, L. C., Mariano, A. J., & Lumpkin, R. (2017). An improved near-surface velocity climatology for the global ocean from drifter observations. *Deep-Sea Research Part I*, *124*, 73–92.

Maximenko, N. A., Bang, B., & Sasaki, H. (2005). Observational evidence of alternating zonal jets in the world ocean. *Geophysical Research Letters*, *32*, L12607. https://doi.org/10.1029/2005GL022728

Maximenko, N. A., Melnichenko, O. V., Niiler, P. P., & Sasaki, H. (2008). Stationary mesoscale jet-like features in the ocean. *Geophysical Research Letters*, *35*, L08603. https://doi.org/10.1029/2008GL033267

McWilliams, J. C. (2008). The nature and consequences of oceanic eddies. In Hecht, M. W. & Hasumi, H. (Eds.), *Ocean modeling in an eddying regime* (pp. 5–15). Washington, DC: American Geophysical Union.

Pedlosky, J. (2013). *Geophysical fluid dynamics*. Berlin, Germany: Springer Science & Business Media.

Rypina, I. I., Kamenkovich, I., Berloff, P., & Pratt, L. J. (2012). Eddy-induced particle dispersion in the near-surface North Atlantic. *Journal of Physical Oceanography*, *42*(12), 2206–2228.

Schlax, M. G., & Chelton, D. B. (2008). The influence of mesoscale eddies on the detection of quasi-zonal jets in the ocean. *Geophysical Research Letters*, *35*, L24602. https://doi.org/10.1029/2008GL035998

Scott, R. B., Arbic, B. K., Holland, C. L., Sen, A., & Qiu, B. (2008). Zonal versus meridional velocity variance in satellite observations and realistic and idealized ocean circulation models. *Ocean Modelling*, *23*(3), 102–112.

Selten, F. M. (1995). An efficient description of the dynamics of barotropic flow. *Journal of the Atmospheric Sciences*, *52*(7), 915–936.

Sirovich, L. (1987a). Turbulence and the dynamics of coherent structures. I. coherent structures. *Quarterly of Applied Mathematics*, *45*(3), 561–571.

Sirovich, L. (1987b). Turbulence and the dynamics of coherent structures. II. symmetries and transformations. *Quarterly of Applied Mathematics*, *45*(3), 573–582.

Stewart, K. D., Spence, P., Waterman, S., Sommer, J. L., Molines, J.-M., Lilly, J., et al. (2015). Anisotropy of eddy variability in the global ocean. *Ocean Modelling*, *95*, 53–65.

Sukoriansky, S., Dikovskaya, N., & Galperin, B. (2007). On the arrest of inverse energy cascade and the Rhines scale. *Journal of the Atmospheric Sciences*, *64*(9), 3312–3327.

Van Sebille, E., Kamenkovich, I., & Willis, J. K. (2011). Quasi-zonal jets in 3-d Argo data of the northeast Atlantic. *Geophysical Research Letters*, *38*, L02606. https://doi.org/10.1029/2010GL046267

Venaille, A., Nadeau, L.-P., & Vallis, G. (2014). Ribbon turbulence. *Physics of Fluids*, *26*(12), 126605.
Von Storch, H., & Zwiers, F. W. (2002). *Statistical analysis in climate research*. Cambridge, UK: Cambridge University Press
Williams, G. P. (1975). Some ocean-Jupiter connections. *Mode News*, *78*, 1–4.
Zang, X., & Wunsch, C. (2001). Spectral description of low-frequency oceanic variability. *Journal of Physical Oceanography*, *31*(10), 3073–3095.

Erratum

In the originally published version of this article, there were several minor errors in figures 14 and 15 and their captions (magnitude of the quantities, mislabeling). All corrections have been made to the online version of this article, but not the PDF, and the online version may be considered the authoritative version of record.

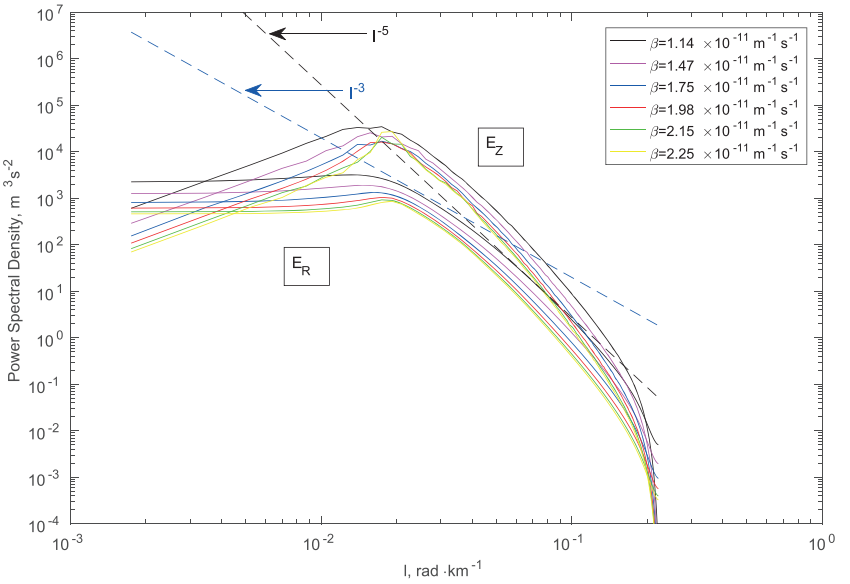

Figure 14. Zonal (E_Z) and residual (E_R) spectra of barotropic kinetic energy for $\gamma=5\times10^{-7}$ s^{-1} and varying β.

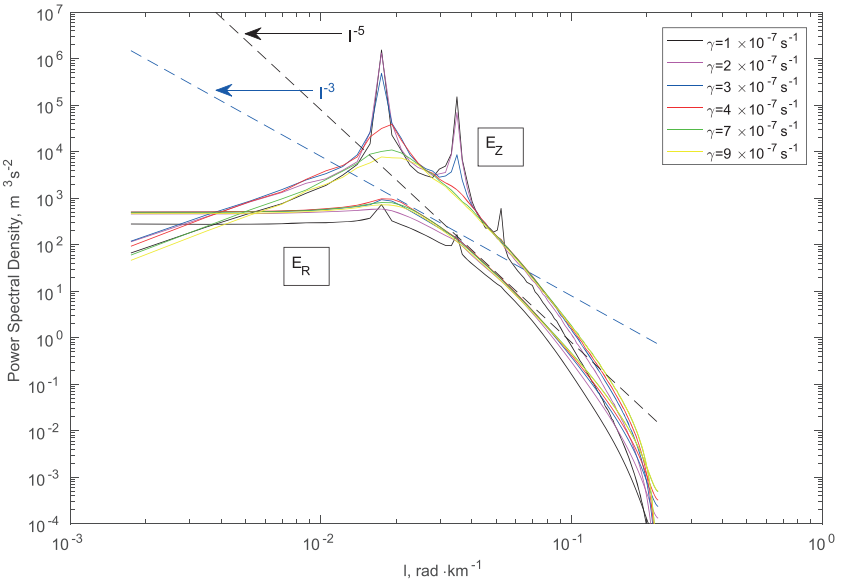

Figure 15. Zonal (E_Z) and residual (E_R) spectra of barotropic kinetic energy for $\beta=2.15\times10^{-11}$ m^{-1} s^{-1} and varying γ.